

promoting access to White Rose research papers



Universities of Leeds, Sheffield and York
<http://eprints.whiterose.ac.uk/>

This is the published version of an article in **Geophysical Journal International**

White Rose Research Online URL for this paper:

<http://eprints.whiterose.ac.uk/id/eprint/78395>

Published article:

Frost, DA, Rost, S, Stuart, GW and Selby, ND (2013) *Detection of a tall ridge at the core-mantle boundary from scattered PKP energy*. *Geophysical Journal International*, 195 (1). 558 - 574. ISSN 0956-540X

<http://dx.doi.org/10.1093/gji/ggt242>

Detection of a tall ridge at the core–mantle boundary from scattered *PKP* energy

Daniel A. Frost,¹ Sebastian Rost,¹ Neil D. Selby² and Graham W. Stuart¹

¹*School of Earth and Environment, University of Leeds, LS2 9JT, UK. E-mail: eedaf@leeds.ac.uk*

²*Blacknest, AWE, Reading, RG7 4RS, UK*

Accepted 2013 June 17. Received 2013 May 21; in original form 2012 October 5

SUMMARY

The seismic wavefield mainly contains reflected, refracted and direct waves but energy related to elastic scattering can also be identified at frequencies of 1 Hz and higher. The scattered, high-frequency seismic wavefield contains information on the small-scale structure of the Earth's crust, mantle and core. Due to the high thermal conductivity of mantle materials causing rapid dissipation of thermal anomalies, the Earth's small-scale structure most likely reveals details of the composition of the interior, and, is therefore essential for our understanding of the dynamics and evolution of the Earth. Using specific ray configurations we can identify scattered energy originating in the lower mantle and under certain circumstances locate its point of origin in the Earth allowing further insight into the structure of the lowermost mantle. Here we present evidence, from scattered *PKP* waves, for a heterogeneous structure at the core–mantle boundary (CMB) beneath southern Africa. The structure rises approximately 80 km above the CMB and is located at the eastern edge of the African LLSVP. Mining-related and tectonic seismic events in South Africa, with m_b from 3.2 to 6.0 recorded at epicentral distances of 119.3° to 138.8° from Yellowknife Array (YKA) (Canada), show large amplitude precursors to *PKP*_{df} arriving 3–15 s prior to the main phase. We use array processing to measure slowness and backazimuth of the scattered energy and determine the scatterer location in the deep Earth. To improve the resolution of the slowness vector at the medium aperture YKA we present a new application of the *F*-statistic. The high-resolution slowness and backazimuth measurements indicate scattering from a structure up to 80 km tall at the CMB with lateral dimensions of at least 1200 km by 300 km, at the edge of the African Large Low Shear Velocity Province. The forward scattering nature of the *PKP* probe indicates that this is velocity-type scattering resulting primarily from changes in elastic parameters. The *PKP* scattering data are in agreement with dynamically supported dense material related to the Large Low Shear Velocity Province.

Key words: Mantle processes; Composition of the mantle; Body waves; Wave scattering and diffraction; Africa.

1 INTRODUCTION

Our current view of the Earth's mantle includes many deviations from a radial 1-D velocity structure on a range of scales. Global tomographic inversions of seismic data elucidate large-scale (on the order of thousands of kilometres) variations in global seismic velocities (e.g. Becker & Boschi 2002). At the other end of the teleseismic frequency spectrum, high-frequency regional studies highlight smaller scale perturbations (on scales of 10–100 km) to 1-D velocity models but are restricted by their limited areal coverage (e.g. Lay & Garnero 2011). Tomographic images of seismic *S*-wave velocities of the lowermost mantle are dominated by large-scale anomalies of reduced velocities relative to the 1-D velocity structure. These regions, called Large Low Shear Velocity Provinces (LLSVP), are located beneath Africa and the Pacific, and are separated by broad

regions of relatively fast mantle, which are geographically correlated with present subduction zones (Castillo 1988; Ritsema *et al.* 1998; Ni *et al.* 2002; Wang & Wen 2007). Therefore the LLSVP and the surrounding fast regions might be a fundamental expression of plate tectonics linking the surface of our planet with its deep interior. Seismic studies of LLSVP indicate an average shear wave velocity reduction of several per cent (Ritsema *et al.* 1998; Ni & Helmberger 2003; Wang & Wen 2007), and several studies indicate sharp boundaries to these structures (Wen 2001; Wen *et al.* 2001). The African LLSVP is likely a dynamic feature of the Earth's deep interior and has been imaged as extending up to 1200 km above the CMB with a bell-shaped cross-section (Ni & Helmberger 2003; Wang & Wen 2007; He & Wen 2009). Geodynamical modelling and seismic results indicate that LLSVP might be thermochemical piles, or upwellings, containing material distinct from the

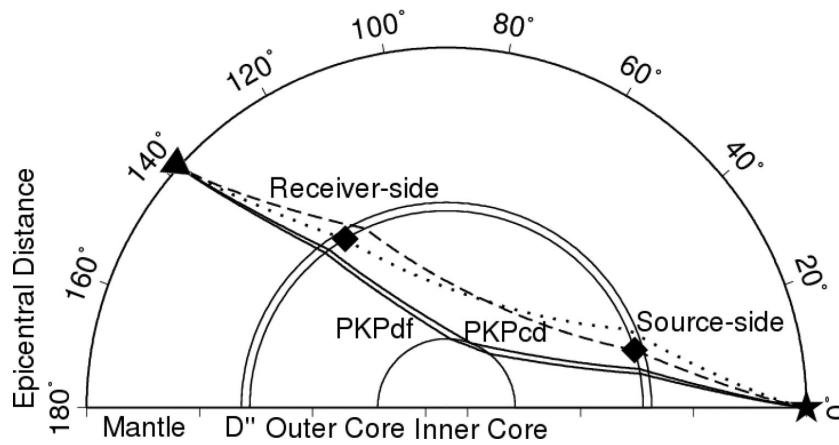


Figure 1. Direct PKP_{df} and PKP_{cd} (solid lines) and source-side scattered P -to- $PKP_{ab/bc}$ and receiver-side scattered $PKP_{ab/bc}$ -to- P (dashed and dotted lines, respectively) for an epicentral distance of 138° . The direct paths PKP_{ab} and PKP_{bc} do not exist at this epicentral distance. The star indicates the source, and diamonds show the scattering points, the triangle represents the receiver.

surrounding mantle (Hart 1984; Creager & Jordan 1986; Young & Lay 1987; Castillo 1988; McNamara & Zhong 2005; Torsvik *et al.* 2006; Wen 2006). Furthermore, LLSVP have been related to large igneous provinces, mantle plumes and hotspot volcanism through upward projection from LLSVP margins corrected for plate motion (Thorne *et al.* 2004; Torsvik *et al.* 2010; Tan *et al.* 2011).

Geodynamical models of LLSVPs as thermochemical piles have been shown to produce small-scale structures, likely related to ultra-low velocity zones (ULVZs), at their margins (McNamara *et al.* 2010; Bower *et al.* 2011) by depositing higher density residual material in areas of stagnant flow at the core–mantle boundary (CMB), which is not entrained in the convective cycle. ULVZs have been observed in many regions of the CMB, often at the periphery of LLSVPs (for an overview of past studies see McNamara *et al.* 2010). They are typically on the order of tens of kilometres in thickness, but exceptionally thick ULVZs of up to 100 km have been reported, with P - and S -wave velocity (V_p and V_s , respectively) decreases of up to 10 per cent and 30 per cent respectively (Williams & Garnero 1996; Wen 2001; Rost *et al.* 2005; To *et al.* 2011). Several studies report drastic density increases of up to 10 per cent (Havens & Revenaugh 2001; Rost *et al.* 2005, 2006).

The seismically imaged 3-D mantle structures have been interpreted as being thermal, chemical or thermochemical in origin (Wright 1975; Doornbos 1978; Garnero 2000). Nonetheless, small-scale heterogeneities with scale-lengths of a few tens of kilometres are most likely of chemical origin due to the high thermal conductivity of the mantle material (Manga & Jeanloz 1996; Becker *et al.* 1999; Turcotte & Schubert 2002). Chemical anomalies may be introduced into the base of the mantle by material flux across the CMB enriching the lower mantle in iron, possibly initiating partial melting (Knittle & Jeanloz 1991; Williams & Garnero 1996; Manga & Jeanloz 1996; Wyssession *et al.* 1998). Alternatively, subducted slabs could descend to and rest at the CMB while slowly mixing into the mantle, possibly on a timescale of billions of years (Christensen & Hofmann 1994; Hirose *et al.* 1999; Dobson & Brodholt 2005; Hutko *et al.* 2006; Cabral *et al.* 2013). Small-scale lateral velocity variations may also be caused by topographical undulations of the CMB surface (Doornbos 1978; Hedlin *et al.* 1997). Given their connection with the large-scale mantle features, studying small-scale heterogeneities is essential for the understanding of mantle dynamics, composition and history of mantle formation and processes.

Seismic energy that cannot be attributed to reflected and refracted phases predicted by standard 1-D earth models, is often attributed to scattered energy produced by the interaction of seismic waves with small-scale heterogeneities (Cleary & Haddon 1972). Waves are scattered at structures of similar scale-length to the incoming wavelength with abrupt contrasts in elastic parameters and/or density. The heterogeneities act as point sources and re-radiate the energy resulting in new, unpredicted, ray paths. Energy arriving before (precursors) and after (post-cursors) main waves such as P , PcP , $P'P'$, $PKKP$, P_{diff} and PKP_{df} has been studied to image the mantle's small-scale structure (Doornbos & Husebye 1972; Husebye *et al.* 1976; Chang & Cleary 1981; Bataille & Flatte 1988; Bataille & Lund 1996; Earle & Shearer 1998; Shearer & Hedlin 1998; Vidale & Hedlin 1998; Thomas *et al.* 1999; Hedlin & Shearer 2000, 2002; Wen 2000; Shearer & Earle 2008; Rost & Earle 2010; Earle *et al.* 2011). For an overview of past studies see Bataille *et al.* (1990) and Shearer (2007).

An often used probe to image the small-scale structure in the lowermost mantle is seismic energy related to PKP (Fig. 1). Due to the sharp seismic velocity decrease across the CMB waves scattered to PKP_{ab} or PKP_{bc} at, or close to, the base of the mantle may arrive at a receiver before the main PKP_{df} and PKP_{cd} branches; this allows separation of lower-mantle scattering (arriving as precursors to PKP_{df}) from shallow scattering processes, for heights less than 800 km above the CMB (arriving as post-cursory energy to PKP_{df} ; Hedlin & Shearer 2002). Waves can be scattered at either the entry or exit point from the core showing similar traveltimes (King *et al.* 1974). However, such waves can be distinguished by measuring the vertical incidence angle, or slowness, with which they arrive at the receiver (Haddon & Cleary 1974). Previous studies have used coherent, high-frequency (1–2 Hz) energy arriving before the core phase PKP_{df} as evidence of relatively small heterogeneous structures scattering waves in the deep mantle (Doornbos & Husebye 1972; King *et al.* 1974; Wright 1975; Husebye *et al.* 1976; Hedlin & Shearer 2000), specifically around the perimeter of the Pacific (Wen & Helmberger 1998; Niu & Wen 2001), in northern Europe (Thomas *et al.* 1999) and in northern North America (Cao & Romanowicz 2007).

A wide variety of seismic array-processing techniques have been developed to allow noise suppression and slowness vector determination through time-series stacking (Rost & Thomas 2002). Due to the low amplitudes of precursors to PKP_{df} , past studies were limited to using relatively large magnitude events ($m_b \geq 5.5$), even when

using seismic arrays (Bataille & Flatte 1988; Wen & Helmberger 1998; Cao & Romanowicz 2007; Thomas *et al.* 2009). Here we introduce an array-processing technique known as the *F*-trace (Blandford 1974) to the study of lowermost mantle scattering; this method will be discussed in detail in Section 3.1. The *F*-trace enables the analysis of very low-magnitude mining-related seismicity (Bowers 2000) in the *PKP* distance region, recorded in north-western Canada, sampling an unstudied region at the edge of the African LLSVP; this will be discussed in Section 2. Using the *F*-trace to process seismic array data dramatically increases the number of sources appropriate for lower-mantle study allowing us to probe previously inaccessible regions for small-scale structure delivering new insights into the chemical and dynamical state of the Earth's interior.

2 DATA

Yellowknife Array (YKA) is an ~20 km aperture, cross-shaped (UK-style) array on the northern shore of the Great Slave Lake (Fig. 2), comprising 18 short-period vertical seismometers with an interstation spacing of 2.5 km arranged in two perpendicular branches, oriented North–South and East–West (Weichert & Whitham 1969). The remote location of this array and simple underlying geology result in extremely low ambient noise conditions, making it well suited to studying high-frequency, small-amplitude *P* waves (Bondar *et al.* 1999).

Intraplate earthquakes from southern Africa (between 30°S to 7°S and 15°E to 35°E) during the time period from 1978 to 2011 recorded at YKA were selected from the data holdings of the Atomic Weapons Establishment (AWE) Blacknest. Data from 1978 to 1990, without magnitude restriction, were taken from analogue

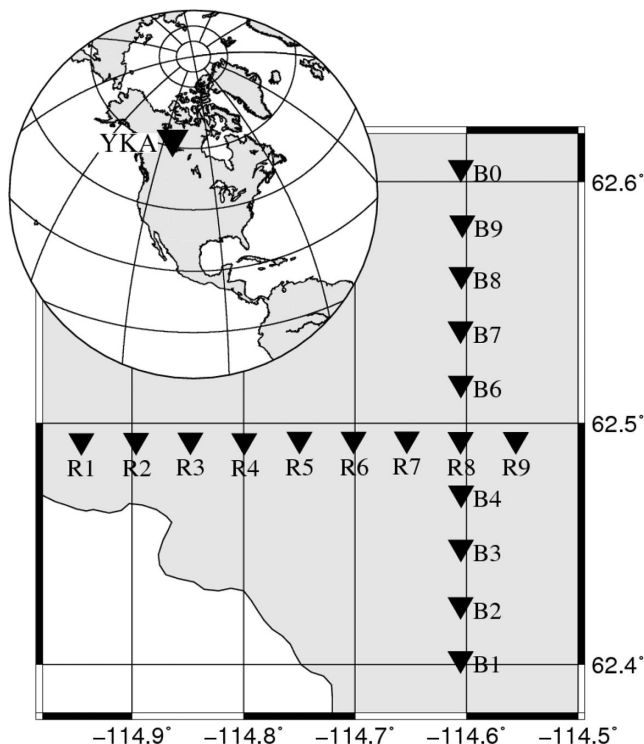


Figure 2. Yellowknife station configuration along two perpendicular N–S; E–W oriented legs. YKA contains 18 stations with a minimum station spacing of 2.5 km and a maximum station separation (aperture) of 20 km. Inset shows Yellowknife Array location in northern Canada.

tapes recently digitized by AWE Blacknest. Although four broadband stations were operating from 1990 onwards, only short-period data are used. We select 153 events from the International Seismological Centre (ISC) catalogues and Comprehensive Nuclear Test Ban Treaty Organisation Reviewed Event Bulletins (REB) with the smallest magnitude (m_b) detected being 3.2 and the largest being 6.0 (Fig. 3a). The majority of the events are related to four deep gold mining regions: the Free State Gold Mines near Welkom, Klerksdorps Gold Mines near Klerksdorp, the Far West Rand Gold Mines near Carletonville and the West and Central Rand Gold Mines near Randfontein (Fig. 3b; see Table S1 for source location details). Waveform modelling of some of these events has previously shown that they are mining-induced seismicity (Bowers 1997). The seismicity from the South African mining region was subdivided into three groups dependent on their association with the Welkom (SW), Klerksdorp (NW) or Carletonville and Randfontein mining regions (NE). The simple source functions (see Fig. S1) and distance to YKA, an array with low noise conditions, makes these events appropriate for study of *PKP* precursors.

3 METHOD

Seismic arrays can be used to determine the slowness vector (composed of the slowness and backazimuth) of an incoming seismic wave front through time-series stacking of the 2-D array record of the wavefield (Davies *et al.* 1971) and improve the signal-to-noise ratio (SNR) of coherent energy over incoherent noise. The resultant stacked trace (beam) shows increased amplitude of seismic energy travelling along the slowness and backazimuth on which it was formed, while energy from other directions is suppressed. The slowness vector represents a directivity vector for the incoming wave front and can be used to locate the origin of the seismic energy.

The aperture of the array, the largest horizontal distance between two seismometers and the number of sites in an array control the resolution to which slowness and backazimuth of the seismic wavefield can be determined. YKA is a medium aperture array, hence it has limited slowness and backazimuth resolution. Stacks of seismograms with different slowness and backazimuth values result in similar beam amplitudes (Figs 4b and 5a), making picking of slowness/backazimuth values for the maximum beam amplitude difficult. For arrays with linear station configurations, such as YKA, energy arriving along the legs of the array leads to spatial aliasing, that is, side-lobes as secondary maxima are formed, reducing precision further (Haubrich 1968).

3.1 *F*-trace array processing

Several methods have been developed to increase slowness/backazimuth resolution (Capon 1969; Neidell and Turhan Taner 1971; Schimmel & Paulssen 1997; Schimmel 1999). For an overview of past studies see Rost & Thomas (2002). In forensic seismology, the *F*-statistic (eq. 1) is used to automatically identify small amplitude arrivals in automatic event detectors (Blandford 1974; Bowers 2000; Selby 2008 2011). Applying the *F*-statistic to a beam, $b(t)$, produces the *F*-statistic trace (*F*-trace), F , which is a dimensionless measure of the beam power divided by the variability (difference) between the beam, $b(t)$, and each trace in the beam, $x_i(t)$, averaged over a box-car time window of width M , normalized by the number of channels used, N (Blandford 1974):

$$F = (N - 1) \frac{N \sum_{t=1}^M b(t)^2}{\sum_{t=1}^M \sum_{i=1}^N (x_i(t) - b(t))^2}. \quad (1)$$

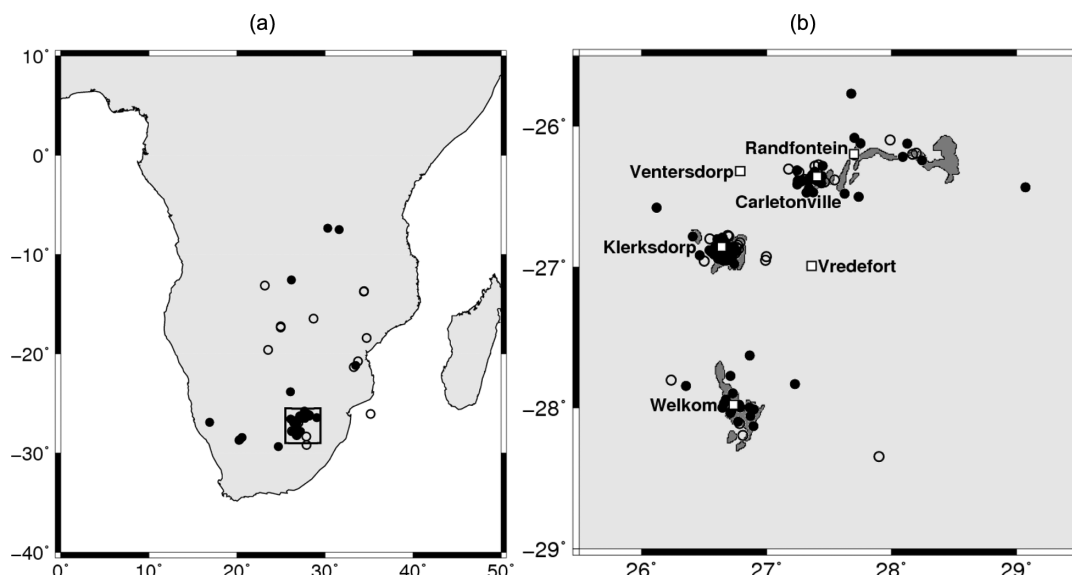


Figure 3. (a) Source locations in southern Africa with category 1 and 2 events as filled circles and category 3 and 4 as open circles showing all events used and the mining region denoted by a black box (see Section 3.2 for category definitions). (b) The mining region with mine areas shaded dark grey and towns as white squares with event location classifications as in (a).

The F -statistic increases the SNR of the beam allowing the analysis of small amplitude arrivals. Here we form beams using the F -statistic for a variety of slownesses and backazimuths in a process called F -packing, and search for the F -trace with the maximum amplitude within a given time window to extract the best fitting slowness and backazimuth for that arrival (Fig. 4a and eq. 2).

$$F_{(\theta,u)} = (N-1) \frac{N \sum_{t=1}^M b_{\theta,u}(t)^2}{\sum_{t=1}^M \sum_{i=1}^N (x_i(t) - b_{\theta,u}(t))^2} \Bigg|_{u=0s \text{ deg}^{-1}}^{u=7s \text{ deg}^{-1}} \Bigg|_{\theta=0^\circ}^{\theta=360^\circ} \quad (2)$$

This technique more heavily penalizes incoherent, and off-azimuth, and slowness arrivals than standard beamforming over a variety of slownesses and backazimuths (beam-packing), or fk -analysis (Capon 1969; Davies *et al.* 1971; Schweitzer *et al.* 2002), hence is more precise in determining the slowness and backazimuth of the incoming wave (Figs 4a and 5).

We apply the F -packing approach to a 30-s time window surrounding PKP_{df} arrivals predicted using IASP91 traveltimes (Kennett & Engdahl 1991). Standard beams and F -traces are calculated for the whole 60 s for a range of slownesses from 0 to 7 s deg^{-1} in 0.1 s deg^{-1} increments and backazimuths from 0° to 360° in 1° increments (Fig. 4b). Data are bandpass filtered using a four-pass, zero phase Butterworth filter with corner frequencies of 1.0 Hz and 2.0 Hz prior to processing. The PKP_{df} arrival is picked by selecting the maximum F -trace amplitude within 1.5 s of the predicted IASP91 time (Fig. 4c). This arrival time is then adjusted to select the strongest arrival, thus accounting for traveltime variations due to 3-D velocity variations. Another phase arriving on average 4.7 s after PKP_{df} can be identified, which is potentially PKP_{cd} , the PKP reflection off the inner core boundary. Despite matching the slowness predicted by IASP91 (Kennett & Engdahl 1991) to within, on average, 0.3 s deg^{-1} , this phase arrives, on average, 2.5 s later than predicted for this distance. This phase may be the result of heterogeneous Earth structure; it will be referred to as PKP_{cd} but is not used in the following analysis and therefore we do not explore its origin further. The majority of events are seen to have one or two precursory phases with distinct slowness and backazimuth values in the F -packs (Fig. 4a).

Due to most events having up to two precursors we restrict our analysis to a maximum of two precursors. These are selected by finding the maximum F -trace amplitude between 8 s and 3 s and then 16 s to 11 s prior to PKP_{df} to allow picking of distinct precursor phases. Traveltimes are picked on the maximum F -statistic and are computed relative to PKP_{df} traveltime to minimize errors due to 3-D velocity structure.

3.2 Data processing and categorization

We categorize events based on the detected arrivals in the F -pack. Category 1 events show both PKP_{df} and PKP_{cd} along with two precursors (56 events in this category, 37 per cent). Category 2 events show PKP_{df} , and one precursor (42 events, 27 per cent). Category 3 contains events in which only PKP_{df} can be observed (18 events, 12 per cent). Category 4 contains events in which there are no identifiable arrivals (37 events, 24 per cent). In the following we use only arrivals from category 1 and 2 events, leaving 98 events (64 per cent of the original population) with 157 precursor detections to be analysed.

3.3 Scatterer location

Slowness, backazimuth and traveltime are used to determine the origin of the scattered energy, and hence the scatterer location within the mantle by ray tracing through a 1-D earth model. Assuming single scattering, source-side scattered energy from the deep mantle will arrive at YKA with slownesses from 2.9 to 4.4 s deg^{-1} , in good agreement with the detected scatterer slownesses (Doornbos & Vlaar 1973; Haddon & Cleary 1974). On the other hand, receiver-side scattering is expected to arrive with slownesses between 1.6 and 3.1 s deg^{-1} , values which are not observed in this data set. Due to the slowness resolution of the processing used, we can rule out the possibility of receiver-side scattering. Other studies (Cao & Romanowicz 2007) identified receiver-side scattering in YKA records from earthquakes in South America; the core exit points of these events are located

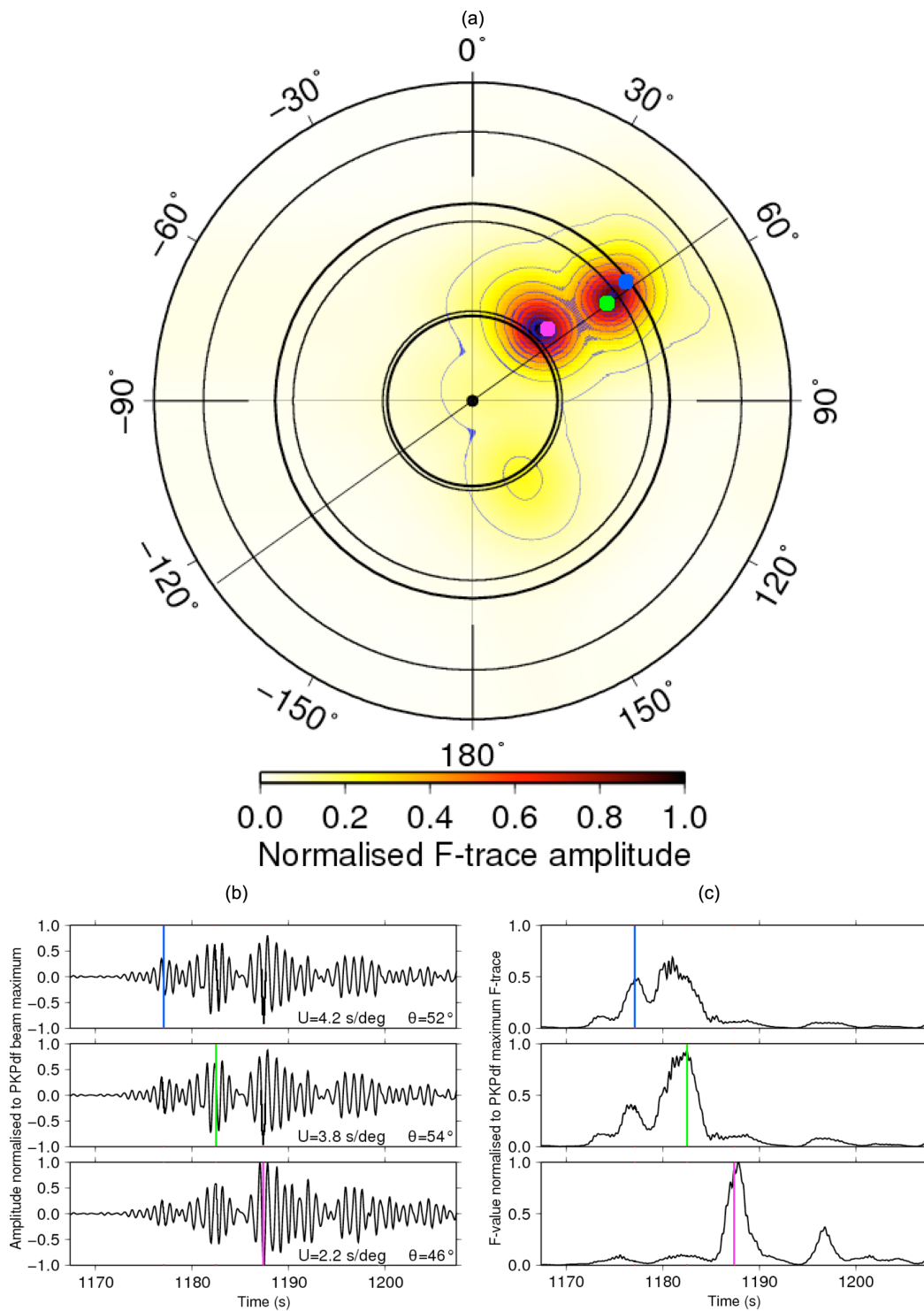


Figure 4. *F*-pack formed by creating beams for backazimuths from -180° to 180° and slownesses of 0.1 to 7.0 s deg^{-1} and calculating the *F*-statistic for each beam, using data recorded at YKA from an event at 22:19:36.77 on 1999 April 22 in South Africa. The *F*-traces are processed with a four-pass, zero phase Butterworth bandpass filter with corner frequencies of 1.0 and 2.0 Hz . Maximum *F*-statistic in a given time window is calculated and all amplitudes are normalized relative to the maximum. (a) Normalized *F*-statistic for a 60 s time window around *PKP*_{df} with peaks identified as the first precursor (blue), second precursor (green) and *PKP*_{df} (pink). Slownesses increase from the centre to the circumference contoured at 2 s deg^{-1} increments. Inner and outer dark contours indicate slownesses of 1.9 and 4.4 s deg^{-1} , representing energy originating in the inner and outer core, respectively. The oblique line indicates the great-circle path. Optimal slownesses (*U*) and backazimuths (θ) used to form the beams (b) and *F*-traces (c) for the first precursor, second precursor and *PKP*_{df} (traces from top to bottom) are shown on each trace and on the *F*-pack as blue, green and pink circles with the lines indicating the picked arrival time for each phase; energy arriving after these comprises the coda.

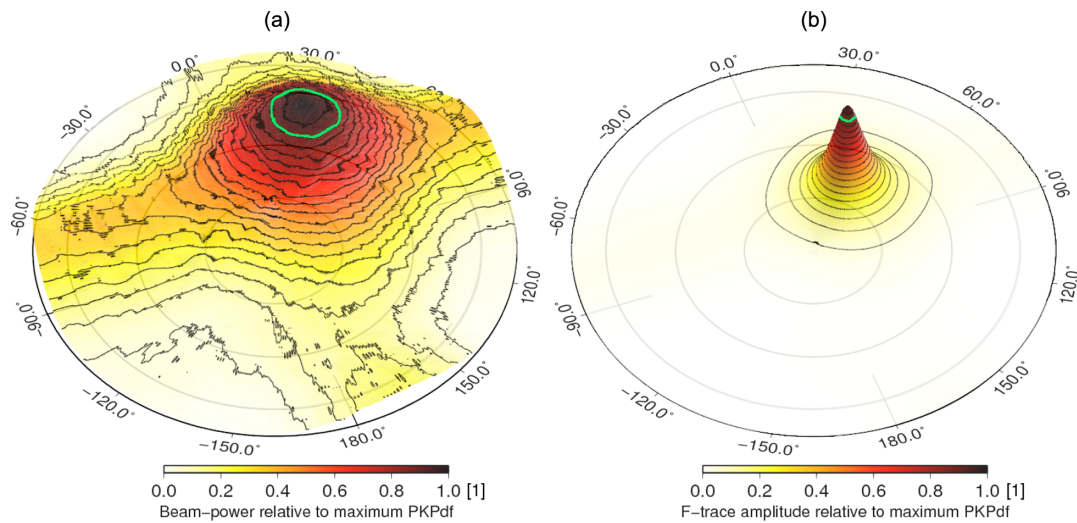


Figure 5. PKP_{df} arrival from the event shown in Fig. 4. (a) Linear beam-pack. (b) F -pack for the same time window showing drastically improved slowness/backazimuth resolution of maximum and suppressed side-lobes. Amplitudes are normalized to the maximum PKP_{df} amplitude and contoured at 0.05. Green contours indicate 90 per cent of the maximum amplitude which for (a) is ± 0.9 s deg^{-1} , $\pm 26^\circ$ relative to the maximum and for (b) is ± 0.2 s deg^{-1} , $\pm 4.5^\circ$ relative to the maximum showing the drastically improved resolution.

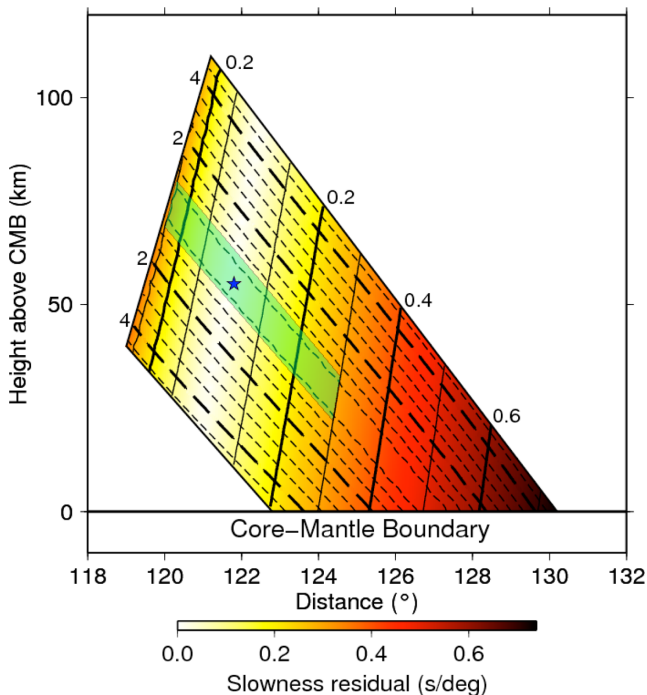


Figure 6. Spatial resolution of potential scatterer location for a surface event at 136.3° distance. Slowness and time misfits are shown as solid and dashed contours, respectively. The grid of potential scatterers is aligned along the backazimuth recorded at YKA. The blue star indicates the best fitting scattering point. The region to which the scattering point is constrained is shown as a green box, with distance uncertainties of $\pm 2^\circ$ and height uncertainties of ± 25 km based on slowness errors of ± 0.25 s deg^{-1} and time errors of ± 0.5 s. Source-to-scatterer distance is best constrained by slowness and scatterer height is best constrained by traveltimes.

beneath central Canada (Cao & Romanowicz 2007) compared to northeast Canada (close to Greenland) in this study. Therefore the sampling of the CMB region is sufficiently different to explain the different results.

Scatterer locations are found by ray tracing through IASP91 (Kennett & Engdahl 1991) from source to receiver via a 3-D grid,

located around the PKP CMB entry point for each individual event. The grid is oriented along the backazimuth measured at YKA with scattering points located between 110° distance from the receiver and the maximum source–receiver distance for each event (i.e. from 119° to 139° giving an average grid spanning 25° along the great circle path) in 0.5° increments, and from the CMB to 200 km above with 5 km vertical spacing (Fig. 6). Preliminary tests with scatterers up to 1200 km above the CMB show that no scattering event can be identified more than 200 km above the CMB in this data set, hence subsequent calculations are limited to heights above the CMB from 0 to 200 km. Ray tracing is performed from source to gridpoint, and gridpoint to receiver. Traveltime, slowness and backazimuth are recorded for each ray path. The best fitting scattering gridpoint is found by minimizing the misfit between observed and modelled slowness and traveltime. Scattering strength at each scattering point is measured by taking the ratio of the maximum F -pack amplitude of the precursor relative to that of PKP_{df} . 39 scatterers (25 per cent of the 157 precursors) cannot be located with sufficiently low misfits on either the source or receiver side. These events are potentially multiple scattered arrivals and are discarded from further analysis.

4 RESULTS

Waveform analysis of PKP_{df} and its precursors shows similar waveforms between the two precursors, PKP_{df} , and the potential PKP_{cd} post-cursor (Fig. 4b and see Fig. S1) indicating that the signals are of related origin. The major phase, PKP_{df} , arrives within ~ 5 s of the time and 0.3 s deg^{-1} of the slowness (with an SD of ± 0.4 s deg^{-1}) predicted by the IASP91 model (Fig. 7; Kennett & Engdahl 1991). PKP_{df} is preceded by several high slowness phases arriving 3–15 s prior to PKP_{df} . Most events show two distinct, time separated precursors with slownesses 2.0 – 1.8 s deg^{-1} higher than PKP_{df} . The earlier precursor generally shows the higher slowness value of the two in each event, and likely originates closer to the CMB. These precursors have clearly defined amplitude peaks and are often separated by a return to background noise levels (Fig. 4). Precursors arrive off great-circle path by up to $\pm 30^\circ$ (average of 7.4° with an SD of 6.7°) for the first (early) precursor and up to $\pm 30^\circ$ (average of 6.0° with an SD of 6.0°) for the second (later) precursor, and

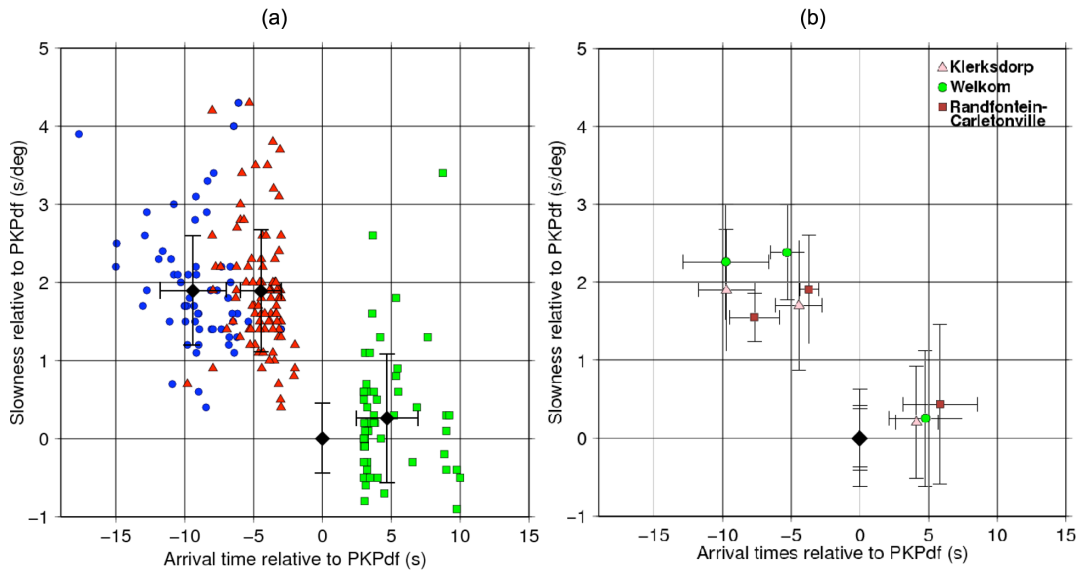


Figure 7. Arrival time and slowness deviations for precursors and PKP_{cd} relative to PKP_{df} (black diamond at 0,0, all time measurements are relative to this phase). (a) Arrivals for all category 1 and 2 events, with first precursors (blue circles), second precursors (red triangles) and PKP_{cd} (green squares). Black diamonds show average arrivals with 1-SD error bars for each phase. Precursors display distinctly different slownesses and arrival times to PKP_{df} . On an event by event basis the slowness of the first precursor is generally greater than that of the second precursor and there is a distinct time gap between the two arrivals. (b) Average arrivals for each phase, for each source region with 1 SD error bars. Green circles, pink triangles and brown squares represent events from Welkom (SW), Klerksdorp (NW) and Carletonville and Randfontein mines (NE), respectively.

hence sample a wider region of the CMB than PKP_{df} . Although these backazimuth deviations are large, theoretical calculations of the backazimuths from the outermost points of the scattering zone (Fig. 10) show that these values are in agreement with the extent of the b -caustic.

The ray tracing results indicate that discrete scatterers reside at heights ranging from the CMB to approximately 80 km above the CMB, with a few outlying scattering points up to 150 km above the CMB. Scattering points, as detected, define a ridge ~ 1200 km long by ~ 300 km wide, trending East–North–East, West–South–West, with modal heights up to 80 km above the CMB (Figs 8a and c). The most elevated scattering points correlate with larger precursor amplitudes relative to PKP_{df} , whereas scatterers closer to the CMB tend to have lower precursor amplitudes (Fig. 8). The area containing scatterers, the scattering volume, is surrounded by weak scattering located on, and just above, the CMB (up to 10 km). There is no evidence of scattering significantly above the CMB in areas other than the ridge indicating strong scattering from this region and less from the surrounding region. Precursor amplitudes relative to PKP_{df} are very high; the average precursor to PKP_{df} amplitude ratio of the first arriving precursors is 0.44 (ranging from 0.1 to 1.90, SD of 0.29), whereas the average second precursor to PKP_{df} amplitude ratio is 0.79 (ranging from 0.20 to 2.50, SD of 0.49). Early first precursors locate closer to the CMB than later second precursors; this agrees with ray tracing results indicating that energy with the largest differential traveltimes relative to PKP_{df} originates from those rays which scatter closest to the CMB. Scatterer distribution is uneven across the study region; however, the centre of the structure is sampled by most source–receiver combinations indicating that the structure is well constrained with multiple data points supporting the resolved features (Fig. 9). Nonetheless, the areas at the periphery of the scattering structure, although less well sampled, are still supported by multiple data points.

Scattering at the CMB in the northeast, south and southwest constrain that the scattering volume tapers off in height towards the

CMB at these edges. However, the northern edge of the scattering structure is not well constrained as the northern extent of the study area is limited by the PKP ray path and the location of the PKP b -caustic (Fig. 10). Inside the sampled region, the scattering ridge height begins to decrease towards the north; however, there are no scatterers recorded at the CMB on this side of the structure. The northern slope of the scattering ridge follows the vertical continuation of the PKP b -caustic (which marks the lower distance limit at which scattering can occur) up from the CMB hence it is possible that the ridge structure may continue in this direction but cannot be detected with this data set (Fig. 10). The elevated areas of the structure will likely cause scattering by both compositional and topographic effects (Bataille *et al.* 1990), whereas the lower areas will mainly scatter through compositional changes, thus generating lower amplitude precursors. Hence the spatial correlation between the elevated scatterers and high-amplitude precursors in the centre of the structure indicates that it is a volumetric heterogeneity with a large velocity and/or density contrast with the surrounding mantle.

To check the robustness of the detected structure against lower quality results we discard all data with SNR (of PKP against background noise before PKP) in the beam less than 5 as synthetic tests show that this is a reasonable noise limit for the F -packing process. Furthermore, to reduce uncertainty in scattering location based on velocity model inaccuracies or picking errors, we remove any scattering points for which the scatterer location process shows misfits in terms of slowness and traveltimes of greater than 0.25 s deg⁻¹ and 1 s, respectively. The strict quality criteria relate to scatterer mislocations of $\pm 2^\circ$ and 60 km (horizontal and vertical, respectively) and can be seen as a stringent test of the reliability of the results. Despite leaving only 41 of the original 157 data points the overall structure of the detected ridge remains very similar (Figs 8c and d).

Some insight into the scattering mechanism of the ridge comes from study of the different earthquake regions of the data set.

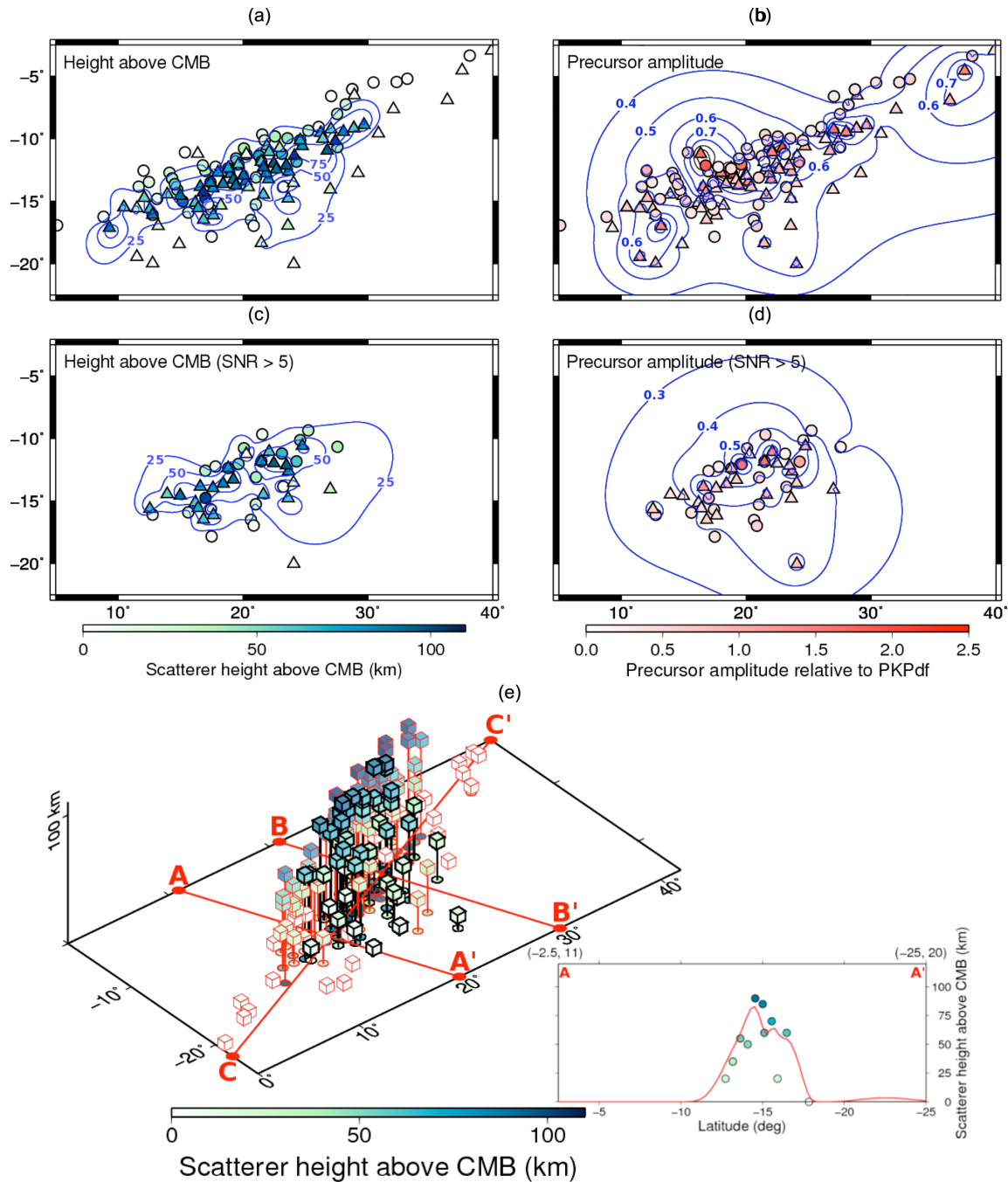


Figure 8. Maps of scatterer locations beneath South Africa where circles and triangles represent the scattering location of first and second precursors, respectively. (a) Scatterer height above the CMB overlaid on a surface of the same data contoured at 25 km intervals. (b) Precursor amplitudes relative to PKP_{df} overlaid on a surface constructed from the same data contoured at 0.1 times PKP_{df} amplitude intervals. (c) Scatterer height above the CMB and (d) precursor amplitude relative to PKP_{df} only showing precursors with beamed SNR larger than 5 and with ray tracing misfits less than 0.25 s^{-1} slowness and 1 s traveltime. This leaves only 41 data points. The surface boundary condition dictates that the scatterers must be at the CMB outside the study region (-1° to 71° longitude, 1° to -26° latitude). (e) Scatterer height above the CMB showing scatterers as discrete points (cubes) forming a cluster of concentrated scattering. Cubes outlined in black satisfy the quality criteria used in (c) and (d) and those outlined in red are of lower quality (SNR < 5, slowness misfit < 0.25 s^{-1} and time misfit < 1 s). The grid is viewed from 220° azimuth inclined at 35° to the plane. Inset shows a cross-section, from A to A', through the scattering volume, between 11° , -2.5° and 20° , -25° , along the red line in the main figure. The red line in the inset shows the height of the scattering surface from (a) along the same section. Scattering points $\pm 1^\circ$ from this line are shown (see Fig. S2 for additional profiles from B to B' and C to C').

Comparison of scattering between the mining areas displays the differences in scattering strength caused by location of the source, whereas comparison between sources in each mining area images the overall variation in scattering strength across the ridge. Despite all three mining source areas having similar event magnitudes,

source to scatterer, and source to receiver distances, the scattering strength recorded varies between them significantly (Fig. 11). Average second precursor to PKP_{df} amplitude ratios range from 1.30 for the Welkom events (SW cluster) to 0.90 for the Carletonville and Randfontein events (NE cluster), and 0.50 for the Klerksdorp

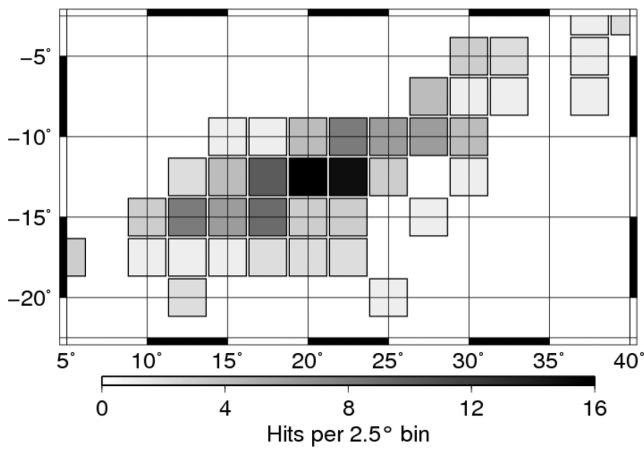


Figure 9. Number of scattering points per 2.5° grid square as symbol shading. Grid squares without scatterers are left blank.

events (NW cluster). Events from the SW cluster tend to scatter on the northern edge of the ridge, the NE cluster events scatter in the middle of the ridge, and the NW cluster events scatter from the northern and southern edges of the ridge. On the other hand, events from the same source cluster sampling the same region of the CMB have similar relative precursor amplitudes with rapid systematic variation with location. Three scattering points from events in the SW cluster are separated by $\leq 1^\circ$ and have an precursor to PKP_{df} average amplitude ratio of 0.40, with a SD of 0.06. Two pairs of scattering points from the NE cluster, separated roughly east–west by $\leq 1^\circ$, both show an increase in amplitude ratio of ~ 0.40 from NW to SW (see Figs S1 and S2). To eliminate any effects due to scattering angle or source variation, we analyse events from the SW cluster with similar backazimuths. Scattering amplitude ratio

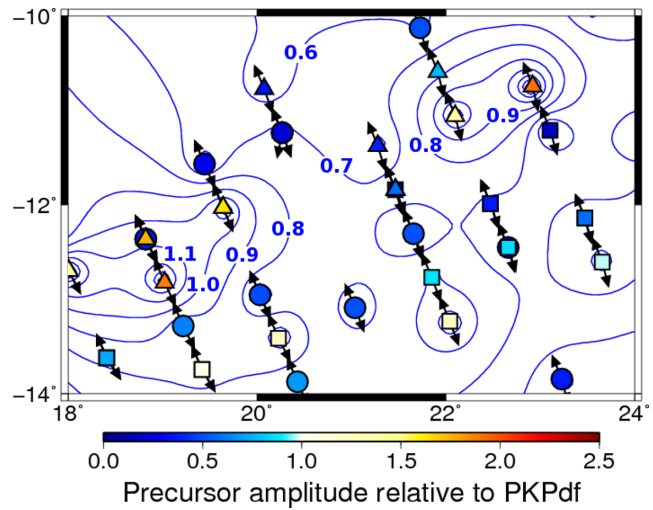


Figure 11. Precursor amplitudes relative to PKP_{df} as in Fig. 8 for the centre of the scattering ridge with the highest scattering point density. Contours are at 0.1 times PKP_{df} amplitude intervals. Precursors are split into mine source regions with events from Welkom (southwest) shown as triangles, from Klerksdorp (northeast) shown as squares and Randfontein and Carletonville (northwest) shown as circles. Arrows show the direction to the source in the southeast and the receiver in the northwest.

increases with distance from 0.40 amplitude in the southeast to 1.60 before decreasing to 1.40 towards the north–northwest over less than 2° distance. This variation is too large to be explained by geometric spreading alone and requires an anomaly that focusses energy differently from SE to NW along the detected ridge (Wright 1975).

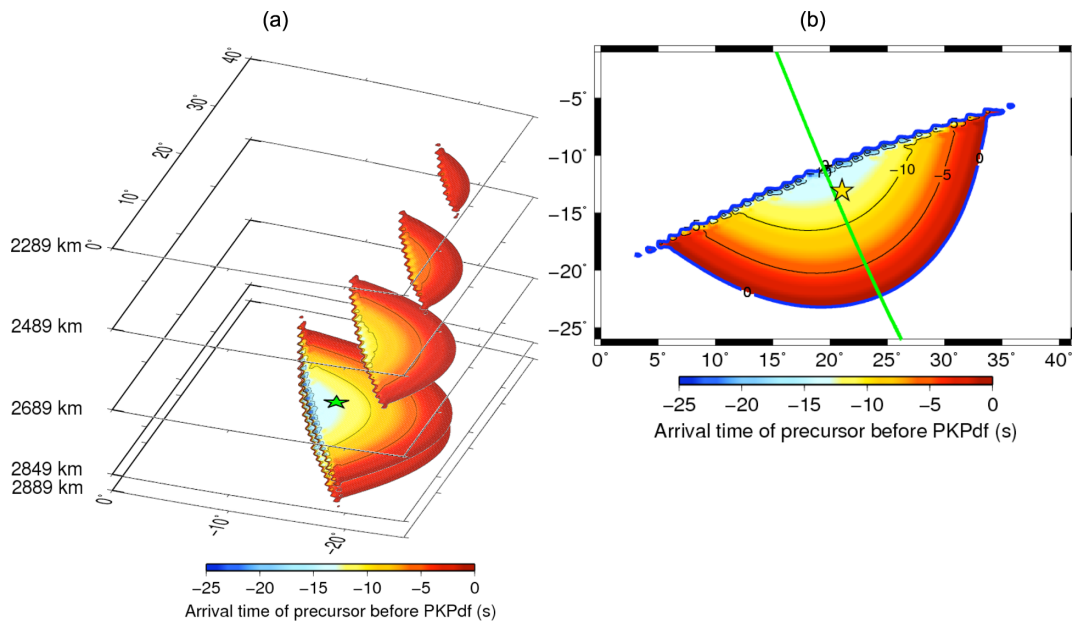


Figure 10. Areas in which scattering generating precursors could occur for an event at 136.2° distance. Colour shows differential traveltimes between PKP_{df} and its precursor contoured at 5 s intervals. Earlier precursors scatter from the northern-most edge of the study region, furthest from the source, close to the CMB. (a) Potential scattering areas at a range of heights from 0 to 600 km above the CMB (depths of 2889–2289 km). This shows the reduction in the area which can generate precursors and the reduction in the time by which scattered energy can precede PKP_{df} with increasing height. The best fitting height (40 km above the CMB) for the precursor to this event is shown with the best fitting scattering point (star). (b) Area at 40 km above the CMB in which scattering generates precursors. The green line shows the great circle path from source to receiver as seen in the data set. The star indicates the best fitting scatterer location for this event, the differential traveltimes between PKP_{df} and this precursor is shown by the symbol colour. All plots are created using a grid with spacing of 0.5° in latitude and longitude.

5 ERROR ANALYSIS

5.1 Azimuth and slowness estimation

To quantify the uncertainties inherent in the F -packing process in determining the slowness and backazimuth for each arrival, synthetic seismograms with varying noise levels are generated and processed. To simulate YKA ambient noise conditions, a trace is taken from YKA for all stations for a time at which no phases arrive according to the catalogues, and no arrivals can be detected when the data are filtered at a range of frequencies (bandpass filters, 0.5 Hz wide, in increments of 0.5 Hz from 0.1 to 3 Hz). Four cosine tapered, 1 Hz sine wavelets, each 2.5 s long, are added to the noise with moveouts (time delays across the array) according to varying slownesses and backazimuths typical of the PKP wave train, using the YKA geometry. Phases are modelled to simulate first and second precursors, PKP_{df} and PKP_{cd} and have slownesses of 4.21, 3.97, 2.17 and 2.27 s deg⁻¹, respectively, and backazimuths of 54°. The first and second arrivals represent precursors and are modelled as having half the amplitude of the third and fourth arrivals representing PKP_{df} and PKP_{cd} . SNR is calculated for each unbeamed trace by creating the envelope and then taking the maximum amplitude in a 3 s time window around the PKP_{df} arrival relative to the maximum amplitude over a 3 s time window before the precursor arrivals. The SNR of the unbeamed traces is varied between 0.005 and 0.5. These are then beamed and filtered, and the SNR of the resulting filtered beam is calculated, varying between 1.9 and 19. To test the accuracy of the F -packing approach the difference between the slowness, backazimuth and traveltimes of the synthetic waveforms, measured through the F -pack in the same way as for the data, is compared to known input values. The misfit is used to indicate the precision of the F -pack with varying signal strength.

SNR values are calculated for all PKP_{df} recordings in the same way as for the synthetic data. Each event category is analysed individually, and category 1, 2 and 3 events are seen to have, on average, SNR values of 10.4, 5.1 and 7.8, respectively. Using synthetics, for a beamed SNR value of 4.6, slowness and backazimuth can be picked to within ± 0.43 s deg⁻¹ and $\pm 7^\circ$ backazimuth. Below this beamed SNR, both slowness and backazimuth picking errors become much larger. For beamed SNR of 12, errors are as low as 0.07 s deg⁻¹ in slowness and 0° in backazimuth. Arrival time residuals for all SNR values and for all phases are up to 1 s, most likely due to the emergent onset of the wavelet, taking this long to reach the maximum wavelet amplitude. This test shows that our F -packing approach is highly accurate at picking the correct slowness, backazimuth and traveltimes despite noisy data. Given the SNR values of the data, the majority of the phases used can be picked to within ~ 0.3 s deg⁻¹ slowness, 0.75 s arrival time and 2° backazimuth.

5.2 Location uncertainty

To estimate the location error related to our ray tracing approach we vary slowness, backazimuth and traveltimes (by up to ± 1 s deg⁻¹, up to $\pm 5^\circ$ and up to ± 2 s, respectively), for a typical scatterer detection, according to the maximum errors determined in Section 5.1 (Fig. 12). Changing the phase arrival time by ± 2 s primarily moves the scatterer vertically by up to 20 km, with later phase arrivals making the scatterer shallower, and earlier phase arrivals making the scatterer deeper. Scatterer location is almost insensitive to changes in slowness of up to ± 0.5 s deg⁻¹. However, scatterer location is most strongly affected by backazimuth modifications, with $\pm 5^\circ$ changes in backazimuth moving the scatterer location by up to $\sim 4.5^\circ$ horizontally and 5 km vertically. Hence backazimuth

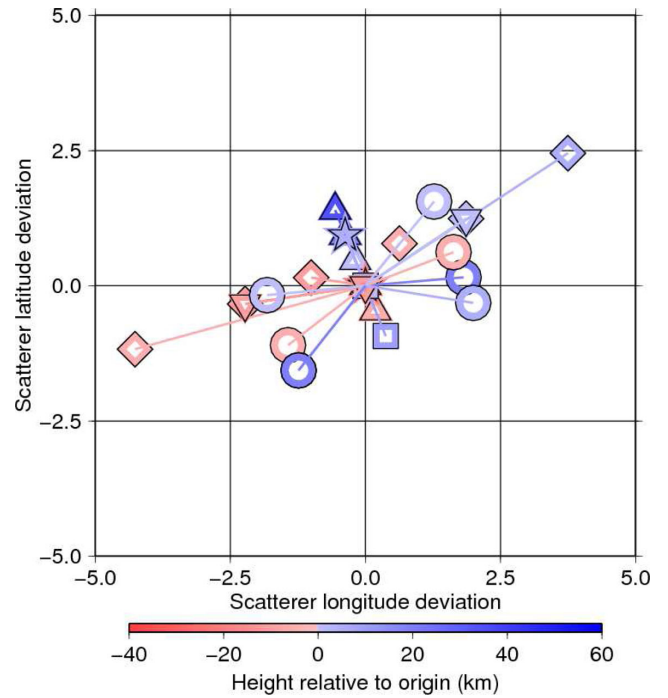


Figure 12. Scatterer locations determined by ray tracing using systematically modified input data, changing slowness, backazimuth and time to simulate the data set. Each scatterer location is plotted relative to that created with the unmodified data thus showing the amount by which changes to each input parameter affect the scatterer location. Changes are made to the input event parameters: latitude and longitude (triangles), picked phase arrival time (stars), picked phase slowness (squares), picked phase backazimuth (diamonds) and arrival time, slowness and backazimuth simultaneously (circles).

is the parameter that must be best determined for good scatterer relocation.

Another source of error might be due to the uncertainty in the published source locations. To test this for the worst possible situations we vary the published source locations by $\pm 2^\circ$ in longitude and latitude, a variation greater than the size of the largest stated error ellipse of the REB source locations. Published error ellipses are up to 136 km long and up to 70 km wide, but on average 13.7 km long (with an SD of 20.7 km) and 8.5 km wide (with an SD of 9.0 km). Source longitude and latitude variations result in the scatterer location at the CMB shifting by up to 1.5° horizontally and 35 km vertically. Slowness, backazimuth and arrival-time errors, of the same size as found in the synthetic tests for an event with SNR ~ 5 , were combined, and the scatterer location deviations were calculated. Using all permutations of ± 0.5 s deg⁻¹, $\pm 2^\circ$ and ± 1 s the scatterer mislocation area was found to be $\sim 4^\circ$ latitude and longitude wide (~ 240 km) and 25 km in height (Fig. 6). Overall the ability to locate scatterers in longitude, latitude and height with the high-accuracy F -trace and the ray tracing backlocation is excellent.

5.3 Stability of detected structure

The robustness of the shape of the scattering structure is assessed by applying a bootstrapping technique to the scattering locations (Efron & Tibshirani 1991). Using all scattering locations we calculate a best fit surface to image the ridge structure. 300 bootstrap realizations are created by randomly sampling 157 scattering points including duplicates from the original 157 scattering points in the data (i.e. the new realization may contain all 157 of the original

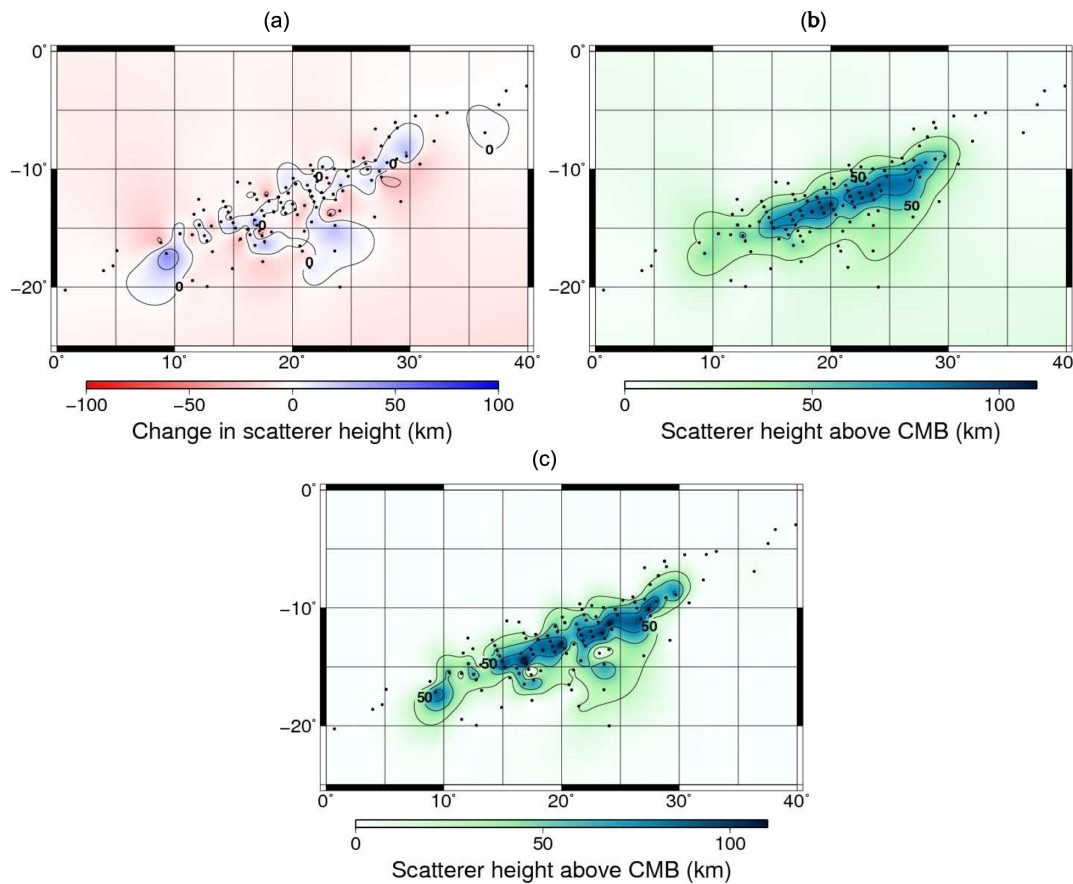


Figure 13. Results of Bootstrap test using 300 realizations. (a) Average of the scatterer height differences between each bootstrap iteration and the original, unsampled grid (as in Fig. 8). (b) Unsampled grid with the average difference subtracted. (c) Unsampled grid (before bootstrapping).

points, or will, more likely, contain fewer unique points but include duplicates totalling to 157). A surface is created for each bootstrap realization. The difference between each point on a regular grid in each bootstrapped surface and the original surface is averaged over all the realizations to calculate the change caused by resampling data, and allows us to test the sensitivity of the scattering structure to specific data points (Fig. 13a). This bootstrapped surface is then subtracted from the original surface thus removing the influence of the least stable elements to reveal the remaining, most stable part of the structure (Fig. 13b). On average the bootstrapped surface is 1.9 km higher than the original, unsampled surface with two outliers decreasing in height by 68 and 41 km, respectively; these points are likely unreliable. The maximum height of the structure is 95 km, defining peaks, above a stable plateau approximately 75 km high; this tapers to the CMB over 120 km laterally to the north and 200 km to the south, and over 750 km to the east and west of the peak. There is no appreciable change in the lateral extent of the structure caused by the bootstrapping process. The structure is smoothed by the bootstrapping process but still remains stable with substantial relief even for the limited data set indicating that the structure is robust and is supported by the majority of the data, and not the result of isolated points.

6 DISCUSSION

Our data indicate structure within the lowermost mantle deviating from standard 1-D earth models. Many mechanisms for the generation of *PKP* precursors have been suggested, such as scattering of

P_{diff} (Bataille & Lund 1996; Thomas *et al.* 2009), scattering of *PKP* by topography on the CMB (Wright 1975) and scattering of *PKP* by volumetric heterogeneity (Doornbos & Husebye 1972).

Energy may be scattered from P_{diff} at the *PKP* *b*-caustic by heterogeneities in the lowermost mantle (Bataille & Lund 1996; Thomas *et al.* 2009). However, 1 Hz waves attenuate to about 1 per cent of their original amplitude within 3° from the *b*-caustic at 143° (Doornbos & Husebye 1972). Diffracted waves could be channelled from the *b*-caustic to the receiver at different distances by a waveguide structure such as a low-velocity zone (Thomas *et al.* 2009). Diffracted precursory waves would then be of a lower frequency than direct PKP_{df} , the reverse of which is seen in these data (see Fig. S4), therefore diffraction is unlikely to explain the precursors in this study.

CMB topography has been proposed as a cause of scattering (Wright 1975). Past amplitude and traveltimes studies have calculated CMB undulations to have a maximum peak-to-peak amplitude of 3 km with wavelengths ≥ 300 km, through inversion of traveltimes of *PcP*, *PKP* and *PKKP* (Menke 1986; Morelli & Dziewonski 1987; Sze & van der Hilst 2003). On smaller scales of ~ 10 km, CMB topography has been modelled as having a rms amplitude of only ~ 300 m (Menke 1986; Earle & Shearer 1997). Structures of this wavelength would generate waves with frequencies above 2 Hz (Vanacore *et al.* 2010), which is greater than the 1–2 Hz dominant frequency of the precursors seen in our data (see Fig. S4) hence this is an unlikely source of the *PKP* scattering and cannot explain scattering up to 80 km above the CMB, the height of which is well constrained through the array processing. However, positive CMB

topography is thought to be indicative of mantle upwellings (Sze & van der Hilst 2003) and our scattering structure matches the location of a 2- to 3-km-tall peak at the CMB, about 1000 km wide, and a -1 per cent velocity decrease (Sze & van der Hilst 2003; Soldati *et al.* 2012). Positive CMB topography may imply that this region of the mantle is upwelling, which could dynamically support anomalous mantle material.

The most likely explanation for this data set is scattering of *PKP* at volumetric heterogeneities, that is, at discrete bodies in the lower mantle with strong velocity or density contrasts, where the scatterer spacing is greater than the incident wavelength (Cao & Romanowicz 2007). As anomalies scatter waves of similar wavelengths to their size, the precursor frequencies imply that scattering is caused by individual anomalies ~ 10 km in size. The precursory wave train observed here is similar to that of other studies of *PKP* scattering where multiple coherent packets of energy, of increasing amplitude, precede PKP_{df} (Doornbos & Husebye 1972; Wen & Helmberger 1998; Hedlin & Shearer 2000; Cao & Romanowicz 2007). This differs from other studies (Hedlin & Shearer 2000), which model scatterers as statistically distributed throughout a mantle volume, that is, scatterers represent statistical scattering volumes generating precursors along the whole ray path. The first arriving waves have travelled the shortest path, that is, the minimum time curve, where the *b*-caustic intersects the CMB at a scatterer–receiver distance of $\sim 117.5^\circ$ (Cleary & Haddon 1972). This wave, which leaves the source with the steepest take-off angle and scatters at the CMB, will spend least time in the relatively slow outer core and hence will arrive earliest, that is, with the largest differential traveltimes relative to PKP_{df} . The minimum scattering traveltimes defines a singular point (Haddon & Cleary 1974), while later arriving energy can scatter from an increasingly large D-shaped region (Fig. 10). For the source–receiver distances of this data set, according to the minimum time curve, the earliest precursors should precede PKP_{df} by 17–13 s depending on epicentral distance. The recorded precursors arrive later than this, implying that they do not scatter from the *b*-caustic, either because there is no heterogeneity along this path, or because the scattered energy is small and below the noise level. Instead they must scatter above the CMB, off-azimuth, or from larger scatterer-to-receiver distances (Fig. 8a).

Recorded slownesses for the direct PKP_{df} and PKP_{cd} waves are consistently ~ 0.2 s deg^{-1} higher than predicted by IASP91 (Kennett & Engdahl 1991) with backazimuths deviating from the great-circle path by on average approximately -5° and 12° , respectively. Slowness deviations are in line with those previously observed at YKA (Bondar *et al.* 1999), which were attributed to local receiver structure. However, the backazimuth deviation of our data is larger and consistently in a different direction than previously determined. The different sign of the PKP_{df} and PKP_{cd} azimuth deviations imply that this is probably due to local receiver structure. The slowness deviation is more likely to be due to 3-D velocity structure within the sampling area (Fig. 10).

The precursor slownesses indicate that the waves are scattered on the source-side before they enter the core (Fig. 7a). However, this does not preclude receiver-side scattering which may still occur (Thomas *et al.* 1999), but these waves, although they are predicted to be of similar amplitudes to source-side energy, may be masked by the source-side waves, which are known to be amplified at certain arrays (Haddon & Cleary 1974). Given the dominance of energy with slownesses indicative of source-side scattering in these data, it implies that the heterogeneities within the scattering volume are much stronger on the source-side than on the receiver-side. The ridge structure scatters waves more effectively than the surrounding man-

tle likely due to a combination of topography and velocity/density heterogeneity. The scattering structure correlates well with a region of the African LLSVP showing a steep velocity gradient, as defined in tomographic images, indicating a link between the large-scale LLSVP and the small-scale mantle structure creating scattering (Fig. 14). However, the apparent strike of the ridge is perpendicular to the sharp eastern boundary of the African LLSVP (Fig. 14 c) previously studied with SKS (Ni *et al.* 2002; Wang & Wen 2004; Helmberger & Ni 2005). There are several interpretations of the exact location of this boundary, and our scattering structure is in general agreement with proposed models. This may be an indication that the resolved structure is only the southernmost end of a larger body which runs further north, parallel with the boundary of the African LLSVP, but this cannot be resolved due to lack of data coverage in this direction.

Backprojection of the location of Large Igneous Provinces, kimberlite and hotspot volcanism to the CMB, corrected for plate motion, implies that they originate close to the -1 per cent ΔV_s contour in the SMEAN tomography model (Becker & Boschi 2002), hence close to the edge of the LLSVP (Torsvik *et al.* 2006 2010; Tan *et al.* 2011). *S*-wave velocity anomaly, and waveform studies (He & Wen 2012) locate the boundary of the Pacific LLSVP in good agreement with the -1 per cent and -1.5 per cent ΔV_s contours in the S40RTS tomography model (Ritsema *et al.* 2010). The best fit for our data seems to be the -0.5 to -1 per cent ΔV_s region, in very good agreement with previous studies mapping the edge of the LLSVP (Figs 14c and d). LLSVPs have been shown in geodynamic models to internally convect (McNamara *et al.* 2010) driving denser residual material to their edges. Hotspots could be the surface expression of entrained dense material caused by the convecting LLSVP, which could draw the heterogeneities upwards where it would be supported by the material beneath. Alternatively, tall heterogeneous piles at the CMB could be produced by dense material carried upwards within the LLSVP, which percolates down along the edges.

Past studies have modelled precursors to PKP_{df} using Chernov's theory for random elastic media or by numerical solution of the acoustic wave equation (Chernov 1960; Vidale & Hedlin 1998; Thomas *et al.* 2000). These studies indicate that a heterogeneous layer with a 5–15 per cent V_p velocity variation with 100–300 km thickness at the base of the mantle is required to generate scattered energy as observed in their data. Modelled velocity parameters are similar to those determined for ULVZs (Williams & Garnero 1996; Revenaugh & Meyer 1997; Rost *et al.* 2005). However, as seen in 1-D synthetics tests, there is a trade-off between anomaly thickness and velocity anomaly within the body where the same scattering and waveform results can be generated by a small volume with a large velocity/density variation or a large volume with a smaller heterogeneity (Husebye *et al.* 1976). Thus thicker layers may actually represent low-velocity zones (LVZs), bodies with lesser velocity and density contrasts than ULVZ, but are significantly thicker than ULVZs (Avants *et al.* 2006). Both structures might be of similar origin. In our data, the height of the scatterers is constrained by the slowness and backazimuth recorded at the array leaving the magnitude of the velocity or density anomaly as the only variable in the modelling. ULVZs have been seen within other parts of the African LLSVP, most often near the margins (Helmberger *et al.* 2000; Ni & Helmberger 2001; Sun *et al.* 2009), and scatterers were detected using a different probe to small-scale structure ($PKKP$) in a similar location to those in this study (Rost & Earle 2010).

Geodynamic modelling (McNamara *et al.* 2010; Bower *et al.* 2011) shows that ULVZs might form elongate structures along the

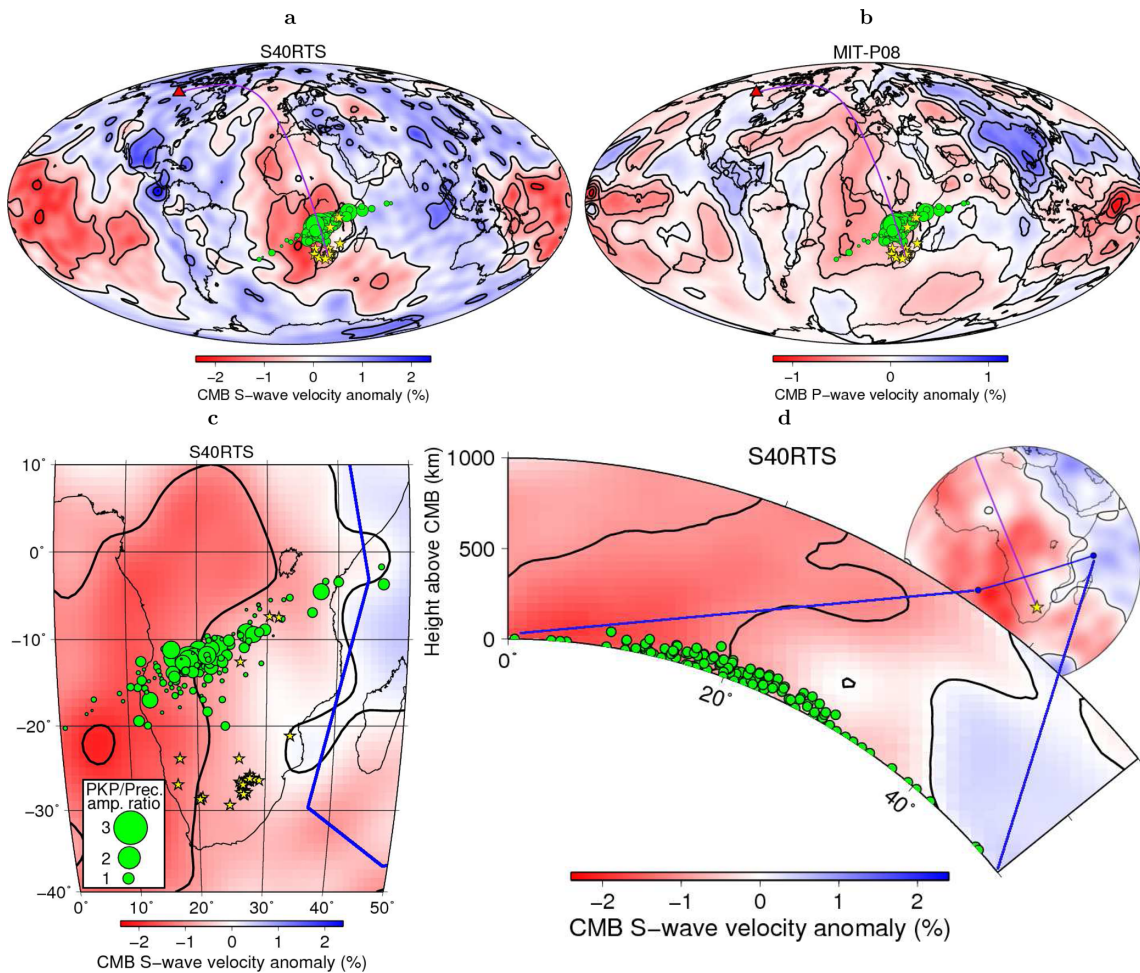


Figure 14. Maps of (a) *S*-wave tomography, at 89 km above the CMB (2800 km depth) using S40RTS, and of (b) *P*-wave tomography, at 20 km above the CMB (2869 km depth), using MIT-P08 with event locations (yellow stars), scattering points (green circles) and a great-circle path (purple) to YKA (red triangle) (Ritsema *et al.* 2010; Li *et al.* 2008). (c) Local *S*-wave tomography structure, at 89 km above the CMB (2800 km depth) using S40RTS, with scatterer locations (symbols are scaled with amplitude relative to PKP_{df}). The blue line indicates the eastern edge of the African LLSVP from Wang & Wen (2004). Precursor amplitudes relative to PKP_{df} are indicated by symbol size. (d) Cross-section through S40RTS from 20°S, 0°E to 50°E, 5°S for heights from the CMB to 1000 km above. Scattering points are projected onto the cross-section line and shown as green circles.

margins of LLSVPs with varying heights. These models indicate that dense material will be transported to the edges of LLSVPs during convection and may pool close to the CMB (McNamara *et al.* 2010). Modelling also suggests that traction dominant flow would generate steep-sided and flat-topped isolated patches of dense material starting from an initially ubiquitous, thin sheet of dense material ($\Delta\rho = +1$ to $+3$ per cent) underlying the mantle, matching ULVZ observations (Wen 2001; Youngs & Houseman 2007 2009). If the scattering volume in this study is composed of mantle material with a density more than 10 per cent greater than ambient mantle as derived in ULVZ studies (Garnero & Helmlberger 1998; Rost & Revenaugh 2003; Rost *et al.* 2005), then it is unlikely that it could maintain a height of 80 km above the CMB without some kind of dynamic or buoyant support (McNamara *et al.* 2010). Taking the aspect ratio of the scattering ridge (height/half-width) this implies a Buoyancy Number (the ratio of chemical to thermal buoyancy) of ~ 1 –2 (McNamara *et al.* 2010; Bower *et al.* 2011). Using the buoyancy number and parameters controlling mantle convection (McNamara *et al.* 2010) gives a density contrast for the anomaly of between $+2.5$ and $+10$ per cent relative to the ambient mantle. Models suggest that a density anomaly of ≥ 5 per cent is required

to prevent entrainment of LVZ material into the LLSVP convection (McNamara *et al.* 2010). If the scattering volume had a density close to or just below this threshold it may allow it to be drawn up along the LLSVP margin but avoid complete destruction by entrainment, explaining the height found here. Despite the smaller density anomaly and, hence, smaller velocity contrast, the thick nature of the body would result in stronger scattering, equivalent to a thinner, denser layer (Wu & Aki 1985). As scattering is caused by discrete velocity anomalies, this implies that the causative structure comprises individual bodies, possibly small pockets of iron-enriched mantle material as has been proposed as the origin for ULVZs (Mao *et al.* 2006; Wicks *et al.* 2010; Bower *et al.* 2011). Waveform studies have found ULVZs 40–300 km tall in association with the edges of LLSVPs indicating that this is not the only occurrence of tall low-velocity anomalies on the Earth (Helmlberger *et al.* 2000; Wen 2001; To *et al.* 2011; Sun *et al.* 2013).

Velocity-type scattering mainly directs scattered energy forwards whereas impedance-type scattering mainly directs scattered energy backwards (Wu & Aki 1985, 1988). These are controlled by changes to the elastic parameters and density, respectively (Sato & Fehler 2008). Precursors to *PKP* require scattering in the forward direction,

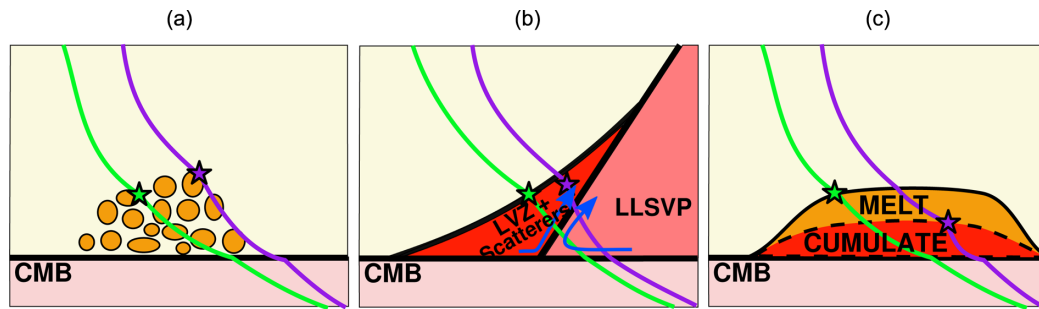


Figure 15. Possible geometries in the lower mantle which may scatter (star) at different heights with (a) an LVZ comprising a collection of random heterogeneities likely included in LLSVP material (not shown), (b) an LVZ over the LLSVP, entrained by internal convection within the LLSVP (blue arrows), (c) or an LVZ with layered internal structure.

through the outer core, hence are likely generated by Velocity-type scattering. This occurs when the changes in elastic parameters and density are of different sign (Wu & Aki 1985) meaning that the scattering body is either stiffer (therefore faster) and less dense or less stiff (therefore slower) and more dense. This agrees well with either a partially molten ULVZ or a solid state Fe-enriched ULVZ (Williams & Garnero 1996; Wicks *et al.* 2010).

Some events (Fig. 3a) do not show scattering and also have a clear time window before PKP_{df} despite being at a similar distance from YKA as events which do show scattering. These events have distances larger than the b -caustic so theoretically could produce PKP precursors through scattering. This implies that the scattering structure is laterally discontinuous, as shown in other studies (Thomas *et al.* 1999; Wen 2000), and strong scattering is not a ubiquitous feature within the lowermost mantle. As the first and second precursors, for the same event, apparently scatter at different heights above the CMB, several scenarios are likely: (1) multiple layers of heterogeneities, or random heterogeneities may be locally concentrated at the edge of the LLSVP (Figs 15a and 8e); (2) LVZs with scatterers could overlie the LLSVP, and sharp transitions between layers from the mantle to the LVZ and then the LVZ to the LLSVP could cause scattering at two heights (Fig. 15b); (3) alternatively, if the LVZ contains a large percentage of melt, below the percolation threshold, then gravitational settling or cumulate precipitation may generate a velocity contrast from mantle to melt, then melt to cumulate (Fig. 15c; Rost *et al.* 2005). The distribution of scatterer heights favours distributed scatterers as there are no specific heights at which scattering of either the first or second precursor seem to cluster, except that the maximum scattering height of around 80–100 km above the CMB is nearly entirely defined by second precursors, and so we favour a combination of the models in Figs 15(a) and (b) with heterogeneities located inside of the LLSVP and being concentrated towards the edge of the larger scale structure. This could indicate that the earlier precursors are produced by scattering from heterogeneities near the CMB and the later, larger amplitude precursors are generated by scattering from the strong topography formed by the pile of heterogeneities at the boundary of the LLSVP.

7 CONCLUSION

The effectiveness of the F -statistic in conjunction with beam-packing in revealing coherent, low-amplitude signals from small-magnitude events offers the opportunity to sample new regions of the CMB with the PKP scattering probe due to the use of low-magnitude earthquakes. Precursors to PKP_{df} from events in South Africa are found to originate from scattering on the source side close

to the CMB beneath southern Africa at the edge of the LLSVP in a region of strong seismic velocity gradients. The scattering volume can be identified as an 80-km-tall ridge trending east-northeast, west–southwest, although some of the boundaries are not well defined and likely not the full structure is being sampled by the data set. The detected ridge is most probably composed of small heterogeneities, approximately 10 km in size, which could be pockets of partial melt, or chemically distinct dense mantle material (e.g. Fe-enriched or dense basaltic remnants) supported by viscous forces at the edge of the LLSVP.

ACKNOWLEDGEMENTS

This work was funded by a NERC studentship. Figures were created using Generic Mapping Tools (Wessel & Smith 1991). Ray tracing was carried out using the TauP Toolkit (Crotwell *et al.* 1999). Data were supplied by AWE Blacknest and the CTBTO. S.R. is partly supported by NERC grant NE/H022473/1.

REFERENCES

- Avants, M., Lay, T. & Garnero, E.J., 2006. A new probe of ULVZ S-wave velocity structure: array stacking of ScS waveforms, *Geophys. Res. Lett.*, **33**(7), 2–5.
- Bataille, K. & Flatte, S.M., 1988. Inhomogeneities near the core-mantle boundary inferred from the Global Digital Seismograph Network, *J. geophys. Res.*, **93**(88), 15 057–15 064.
- Bataille, K. & Lund, F., 1996. Strong scattering of short-period seismic waves by the core-mantle boundary and the P -diffracted Wave, *Geophys. Res. Lett.*, **23**(18), 2413–2416.
- Bataille, K., Wu, R.S. & Flatte, S.M., 1990. Inhomogeneities near the core-mantle boundary evidenced from scattered waves: a review, *Pure appl. Geophys.*, **132**, 151–173.
- Becker, T.W. & Boschi, L., 2002. A comparison of tomographic and geodynamic mantle models, *Geochem. Geophys. Geosyst.*, **3**(1), doi:10.1029/2001GC000168.
- Becker, T.W., Kellogg, J.B. & Connell, R.J.O., 1999. Thermal constraints on the survival of primitive blobs in the lower mantle, *Earth planet. Sci. Lett.*, **171**, 351–365.
- Blandford, R.R., 1974. An automatic event detector at the Tonto Forest seismic observatory, *Geophysics*, **39**, 633–643.
- Bondar, I., North, R.G. & Beall, G., 1999. Teleseismic slowness-azimuth station corrections for the International Monitoring System seismic network, *Bull. seism. Soc. Am.*, **89**, 989–1003.
- Bowers, D., 1997. The October 30, 1994, seismic disturbance in South Africa: earthquake or large rock burst? *J. geophys. Res.*, **102**, 9843–9857.
- Bowers, D., 2000. Using the F-Detector to help interpret P-seismograms recorded by seismometer arrays, in *Proceedings of Seismic Res. Symp.*, New Orleans, USA, p. 10.

- Bower, D.J., Wicks, J.K., Gurnis, M. & Jackson, J.M., 2011. A geodynamic and mineral physics model of a solid-state ultralow-velocity zone, *Earth planet. Sci. Lett.*, **303**, 193–202.
- Cabral, R.A. *et al.*, 2013. Anomalous sulphur isotopes in plume lavas reveal deep mantle storage of Archaean crust, *Nature*, **496**(7446), 490–493.
- Cao, A. & Romanowicz, B., 2007. Locating scatterers in the mantle using array analysis of PKP precursors from an earthquake doublet, *Earth planet. Sci. Lett.*, **255**, 22–31.
- Capon, J., 1969. High-resolution frequency-wavenumber spectrum analysis, *Proc. IEEE*, **57**, 1408–1418.
- Castillo, P., 1988. The Dupal anomaly as a trace of the upwelling lower mantle, *Nature*, **336**, 667–670.
- Chang, A.C. & Cleary, J.R., 1981. Scattered PKKP: further evidence for scattering at a rough core-mantle boundary, *Phys. Earth planet. Int.*, **24**, 15–29.
- Chernov, L.A., 1960. *Wave Propagation in a Random Medium*, McGraw-Hill Book Company, New York.
- Christensen, U.R. & Hofmann, A.W., 1994. Segregation of subducted oceanic crust in the convecting mantle isotope ratios strongly with R, the ratio of chemical to thermal moderately with the Rayleigh number R_a , where Yuen found, *J. geophys. Res.*, **99**, 19 867–19 844.
- Cleary, J.R. & Haddon, R.A.W., 1972. Seismic wave scattering near the core-mantle boundary: a new interpretation of precursors to PKP, *Nature*, **240**, 549–551.
- Creager, K.C. & Jordan, T.H., 1986. Slab penetration into the lower mantle beneath the Mariana and other island arcs of the northwest Pacific, *J. geophys. Res.-Solid Earth*, **91**, 3573–3589.
- Crotwell, H.P., Owens, T.J. & Ritsema, J., 1999. The TauP toolkit: flexible seismic travel-time and raypath utilities, *Seismol. Res. Lett.*, **70**, 154–160.
- Davies, D., Kelly, E.J. & Filson, J.R., 1971. Vespa process for analysis of seismic signals, *Nat. Phys. Sci.*, **232**, 8–13.
- Dobson, D.P. & Brodholt, J.P., 2005. Subducted banded iron formations as a source of ultralow-velocity zones at the core mantle boundary, *Nature*, **434**, 371–374.
- Doornbos, D.J., 1978. On seismic-wave scattering by a rough core-mantle boundary, *Geophys. J. R. astr. Soc.*, **53**, 643–662.
- Doornbos, D.J. & Husebye, E.S., 1972. Array analysis of PKP phases and their precursors, *Phys. Earth planet. Inter.*, **5**, 387–399.
- Doornbos, D.J. & Vlaar, N.J., 1973. Regions of seismic wave scattering in the Earth's mantle and precursors to PKP, *Nat. Phys. Sci.*, **243**, 58–61.
- Earle, P.S. & Shearer, P.M., 1997. Observations of PKKP precursors used to estimate small-scale topography on the core-mantle boundary, *Science*, **277**, 667–670.
- Earle, P.S. & Shearer, P.M., 1998. Observations of high-frequency scattered energy associated with the core phase PKKP, *Geophysics*, **25**, 405–408.
- Earle, P.S., Rost, S., Shearer, P.M. & Thomas, C., 2011. Scattered P'P' waves observed at short distances, *Bull. seism. Soc. Am.*, **101**, 2843–2854.
- Efron, B. & Tibshirani, R., 1991. Statistical data analysis in the computer age, *Science*, **253**(5018), 390–395.
- Garnero, E.J., 2000. Heterogeneity of the lowermost mantle, *Ann. Rev. Earth planet. Sci.*, **28**, 509–539.
- Garnero, E.J. & Helmberger, D.V., 1998. Further structural constraints and uncertainties of a thin laterally varying ultralow-velocity layer at the base of the mantle, *J. geophys. Res.*, **103**(B6), 12 495–12 509.
- Haddon, R.A.W. & Cleary, J.R., 1974. Evidence for scattering of seismic PKP waves near the mantle-core boundary, *Phys. Earth planet. Inter.*, **8**, 211–234.
- Hart, S.R., 1984. A large-scale isotope anomaly in the Southern Hemisphere mantle, *Nature*, **309**, 753–757.
- Haubrich, R.A., 1968. Array design, *Bull. seism. Soc. Am.*, **58**(3), 977–991.
- Havens, E. & Revenaugh, J., 2001. A broadband seismic study of the lowermost mantle beneath Mexico: constrains on ultralow velocity zone elasticity and density, *J. geophys. Res.*, **106**, 30 809–30 820.
- He, Y. & Wen, L., 2009. Structural features and shear-velocity structure of the Pacific Anomaly, *J. geophys. Res.*, **114**, 1–17.
- He, Y. & Wen, L., 2012. Geographic boundary of the Pacific Anomaly and its geometry and transitional structure in the north, *J. geophys. Res.*, **117**(B9), 1–16.
- Hedlin, M.A.H. & Shearer, P.M., 2000. An analysis of large-scale variations in small-scale mantle heterogeneity using Global Seismographic Network recordings of precursors to PKP, *J. geophys. Res.*, **105**(B6), 13 655–13 673.
- Hedlin, M.A.H. & Shearer, P.M., 2002. Probing mid-mantle heterogeneity using PKP coda waves, *Phys. Earth planet. Inter.*, **130**, 195–208.
- Hedlin, M.A.H., Shearer, P.M. & Earle, P.S., 1997. Seismic evidence for small-scale heterogeneity throughout the Earth's mantle, *Nature*, **387**, 145–150.
- Helmberger, D.V. & Ni, S., 2005. Seismic modeling constraints on the South African super plume, in *Earth's Deep Mantle: Structure, Composition, and Evolution*, pp. 63–81, American Geophysical Union.
- Helmberger, D., Ni, S., Wen, L. & Ritsema, J., 2000. Seismic evidence for ultralow-velocity zones beneath Africa and eastern Atlantic, *J. geophys. Res.*, **105**, 865–878.
- Hirose, K., Fei, Y., Ma, Y. & Mao, H., 1999. The fate of subducted basaltic crust in the Earth's lower mantle, *Nature*, **397**, 53–56.
- Husebye, E.S., King, D.W. & Haddon, R.A.W., 1976. Precursors to PKIKP and seismic wave scattering near the mantle-core boundary, *J. geophys. Res.*, **81**(11), 1870–1882.
- Hutko, A.R., Lay, T., Garnero, E.J. & Revenaugh, J., 2006. Seismic detection of folded, subducted lithosphere at the core-mantle boundary, *Nature*, **441**, 333–6.
- Kennett, B.L.N. & Engdahl, E.R., 1991. Traveltimes for global earthquake location and phase identification, *Geophys. J. Int.*, **105**, 429–465.
- King, D.W., Haddon, R.A.W. & Cleary, J.R., 1974. Array analysis of precursors to PKIKP in the distance range 128 to 142, *Geophys. J. R. astr. Soc.*, **37**, 157–173.
- Knittle, E. & Jeanloz, R., 1991. Earth's core-mantle boundary: results of experiments at high pressures and temperatures, *Science*, **251**, 1431–1443.
- Lay, T. & Garnero, E.J., 2011. Deep mantle seismic modeling and imaging, *Ann. Rev. Earth planet. Sci.*, **39**, 91–123.
- Li, C., van der Hilst, R.D., Engdahl, E.R. & Burdick, S., 2008. A new global model for P wave speed variations in Earth's mantle, *Geochem. Geophys. Geosyst.*, **9**(5), Q05018, doi:10.1029/2007GC001806.
- Manga, M. & Jeanloz, R., 1996. Implications of a metal-bearing chemical boundary layer in D'' for mantle dynamics, *Geophys. Res. Lett.*, **23**, 3091–3094.
- Mao, W.L. *et al.*, 2006. Iron-rich post-perovskite and the origin of ultralow-velocity zones, *Science*, **312**, 564–565.
- McNamara, A.K. & Zhong, S., 2005. Thermochemical structures beneath Africa and the Pacific Ocean., *Nature*, **437**, 1136–1139.
- McNamara, A.K., Garnero, E.J. & Rost, S., 2010. Tracking deep mantle reservoirs with ultra-low velocity zones, *Earth planet. Sci. Lett.*, **299**, 1–9.
- Menke, W., 1986. Few 2–50 km corrugations on the core-mantle boundary, *Geophys. Res. Lett.*, **13**, 1501–1504.
- Morelli, A. & Dziewonski, A.M., 1987. Topography of the core-mantle boundary and lateral homogeneity of the liquid core, *Nature*, **325**, 678–683.
- Neidell, N.S. & Turhan Taner, M., 1971. Semblance and other coherency measures for multichannel data, *Geophysics*, **36**(3), 482–497.
- Ni, S. & Helmberger, D.V., 2001. Probing an ultra-low velocity zone at the core-mantle boundary with P and S waves, *Geophys. Res. Lett.*, **28**, 2345–2348.
- Ni, S. & Helmberger, D.V., 2003. Ridge-like lower mantle structure beneath South Africa, *J. geophys. Res.*, **108**, 1–14.
- Ni, S., Tan, E., Gurnis, M. & Helmberger, D., 2002. Sharp sides to the African superplume, *Science*, **296**, 1850–1852.
- Niu, F. & Wen, L., 2001. Strong seismic scatterers near the core-mantle boundary west of Mexico, *Geophys. Res. Lett.*, **28**, 3557–3560.
- Revenaugh, J. & Meyer, R., 1997. Seismic evidence of partial melt within a possibly ubiquitous low-velocity layer at the base of the mantle, *Science*, **277**, 670–673.
- Ritsema, J., Ni, S., Helmberger, D.V. & Crotwell, H.P., 1998. Evidence for strong shear velocity reductions and velocity gradients in the lower mantle beneath Africa, *Geophys. Res. Lett.*, **25**, 4245–4248.

- Ritsema, J., Deuss, A., van Heijst, H.J. & Woodhouse, J.H., 2010. S40RTS: a degree-40 shear-velocity model for the mantle from new Rayleigh wave dispersion, teleseismic traveltime and normal-mode splitting function measurements, *Geophys. J. Int.*, **184**, 1223–1236.
- Rost, S. & Earle, P.S., 2010. Identifying regions of strong scattering at the core-mantle boundary from analysis of PKKP precursor energy, *Earth planet. Sci. Lett.*, **297**, 616–626.
- Rost, S. & Revenaugh, J., 2003. Small-scale ultralow-velocity zone structure imaged by ScP, *J. geophys. Res.*, **108**, 1–10.
- Rost, S. & Thomas, C., 2002. Array seismology: methods and applications, *Rev. Geophys.*, **40**, 1–27.
- Rost, S., Garnero, E.J., Williams, Q. & Manga, M., 2005. Seismological constraints on a possible plume root at the core-mantle boundary, *Nature*, **435**, 666–669.
- Rost, S., Garnero, E.J. & Williams, Q., 2006. Fine-scale ultralow-velocity zone structure from high-frequency seismic array data, *J. geophys. Res.*, **111**, 1–14.
- Sato, H. & Fehler, M.C., 2008. *Seismic Wave Propagation and Scattering in the Heterogeneous Earth*, 2nd edn, Springer Verlag and AIP Press, New York.
- Schimmel, M., 1999. Phase cross-correlations: design, comparisons, and applications, *Bull. seism. Soc. Am.*, **89**, 1366–1378.
- Schimmel, M. & Paulssen, H., 1997. Noise reduction and detection of weak, coherent signals through phase-weighted stacks, *Geophys. J. Int.*, **130**, 497–505.
- Schweitzer, J., Fyen, J., Mykkeltveit, S. & Kvaerna, T., 2002. Seismic arrays, in *New Manual of Seismological Observatory Practice*, Vol. 1, pp. 481–532, ed. Bormann, P., IASPEI.
- Selby, N.D., 2008. Application of a generalized F detector at a seismometer array, *Bull. seism. Soc. Am.*, **98**, 2469–2481.
- Selby, N.D., 2011. Improved teleseismic signal detection at small-aperture arrays, *Bull. seism. Soc. Am.*, **101**, 1563–1575.
- Shearer, P.M., 2007. Seismic scattering in the deep Earth, in *Treatise on Geophysics*, Vol. 1: Deep Earth Structure, pp. 695–730, ed., Schubert, G., Elsevier Ltd., Oxford.
- Shearer, P.M. & Earle, P.S., 2008. Observing and modeling elastic scattering in the deep earth, *Adv. Geophys.*, **50**, 167–193.
- Shearer, P.M., Hedlin, M.A.H. & Earle, P.S., 1998. PKP and PKKP precursor observations: Implications for the small-scale structure of the deep mantle and core, in *The Core-Mantle Boundary Region*, Geodynamics Series, Vol. 28, pp. 37–55, AGU, Washington, DC.
- Soldati, G., Boschi, L. & Forte, A.M., 2012. Tomography of core-mantle boundary and lowermost mantle coupled by geodynamics, *Geophys. J. Int.*, **189**, 730–746.
- Sun, D., Helmberger, D., Ni, S. & Bower, D., 2009. Direct measures of lateral velocity variation in the deep Earth, *J. geophys. Res.*, **114**, 1–18.
- Sun, D., Helmberger, D.V., Jackson, J.M., Clayton, R.W. & Bower, D.J., 2013. Rolling hills on the core–mantle boundary, *Earth planet. Sci. Lett.*, **361**, 333–342.
- Sze, E.K.M. & van der Hilst, R.D., 2003. Core mantle boundary topography from short period PcP, PKP, and PKKP data, *Phys. Earth planet. Inter.*, **135**, 27–46.
- Tan, E., Leng, W., Zhong, S. & Gurnis, M., 2011. On the location of plumes and lateral movement of thermochemical structures with high bulk modulus in the 3-D compressible mantle, *Geochem. Geophys. Geosyst.*, **12**, 1–13.
- Thomas, C., Weber, M., Wicks, C.W. & Scherbaum, F., 1999. Small scatterers in the lower mantle observed at German broadband arrays, *J. geophys. Res.*, **104**(B7), 15 073–15 088.
- Thomas, C., Igel, H., Weber, M. & Scherbaum, F., 2000. Acoustic simulation of P-wave propagation in a heterogeneous spherical Earth: numerical method and application to precursor waves to PKPdf, *Geophys. J. Int.*, **141**, 307–320.
- Thomas, C., Kendall, J.M. & Helffrich, G., 2009. Probing two low-velocity regions with PKP b-caustic amplitudes and scattering, *Geophys. J. Int.*, **178**, 503–512.
- Thorne, M., Garnero, E.J. & Grand, S.P., 2004. Geographic correlation between hot spots and deep mantle lateral shear-wave velocity gradients, *Phys. Earth planet. Inter.*, **146**, 47–63.
- To, A., Fukao, Y. & Tsuboi, S., 2011. Evidence for a thick and localized ultra low shear velocity zone at the base of the mantle beneath the central Pacific, *Phys. Earth planet. Inter.*, **184**, 119–133.
- Torsvik, T.H., Smethurst, M.A., Burke, K. & Steinberger, B., 2006. Large igneous provinces generated from the margins of the large low-velocity provinces in the deep mantle, *Geophys. J. Int.*, **167**, 1447–1460.
- Torsvik, T.H., Burke, K., Steinberger, B., Webb, S.J. & Ashwal, L.D., 2010. Diamonds sampled by plumes from the core-mantle boundary, *Nature*, **466**, 352–355.
- Turcotte, D.L. & Schubert, G., 2002. *Geodynamics Applications of Continuum Physics to Geological Problems*, 2nd edn, John Wiley & Sons, Inc., New York.
- Vanacore, E., Niu, F. & Ma, Y., 2010. Large angle reflection from a dipping structure recorded as a PKIKP precursor: evidence for a low velocity zone at the core–mantle boundary beneath the Gulf of Mexico, *Earth planet. Sci. Lett.*, **293**, 54–62.
- Vidale, J.E. & Hedlin, M.A.H., 1998. Evidence for partial melt at the core–mantle boundary north of Tonga from the strong scattering of seismic waves, *Nature*, **391**, 682–685.
- Wang, Y. & Wen, L., 2004. Mapping the geometry and geographic distribution of a very low velocity province at the base of the Earth’s mantle, *J. geophys. Res.*, **109**(B10), B10305, doi:10.1029/2003JB002674.
- Wang, Yi & Wen, L., 2007. Geometry and P and S velocity structure of the African Anomaly, *J. geophys. Res.*, **112**, 1–26.
- Weichert, D.H. & Whitham, K., 1969. Calibration of the Yellowknife Seismic Array with first zone explosions, *Geophys. J. R. astr. Soc.*, **18**, 461–476.
- Wen, L., 2000. Intense seismic scattering near the Earth’s core-mantle boundary beneath the Comoros hotspot, *Geophys. Res. Lett.*, **27**(22), 3627–3630.
- Wen, L., 2001. Seismic evidence for a rapidly varying compositional anomaly at the base of the Earth’s mantle beneath the Indian Ocean, *Earth planet. Sci. Lett.*, **194**, 83–95.
- Wen, L., 2006. A compositional anomaly at the Earth’s core–mantle boundary as an anchor to the relatively slowly moving surface hotspots and as source to the DUPAL anomaly, *Earth planet. Sci. Lett.*, **246**, 138–148.
- Wen, L. & Helmberger, D.V., 1998. Ultra-low velocity zones near the core-mantle boundary from broadband PKP precursors, *Science*, **279**, 1701–1703.
- Wen, L., Silver, P., James, D. & Kuehnel, R., 2001. Seismic evidence for a thermo-chemical boundary at the base of the Earth’s mantle, *Earth planet. Sci. Lett.*, **189**, 141–153.
- Wessel, P. & Smith, W.H.F., 1991. Free software helps map and display data, *EOS Trans.*, **72**, 441–448.
- Wicks, J.K., Jackson, J.M. & Sturhahn, W., 2010. Very low sound velocities in iron-rich (Mg,Fe)O: implications for the core-mantle boundary region, *Geophys. Res. Lett.*, **37**, 1–5.
- Williams, Q. & Garnero, E.J., 1996. Seismic evidence for partial melt at the base of Earth’s mantle, *Science*, **273**, 1528–1530.
- Wright, C., 1975. The origin of short-period precursors to PKP, *Bull. seism. Soc. Am.*, **65**, 765–786.
- Wu, R.-S. & Aki, K., 1985. Scattering characteristics of elastic waves by an elastic heterogeneity, *Geophysics*, **50**, 582–595.
- Wu, R. & Aki, K., 1988. Introduction: seismic wave scattering in three-dimensionally heterogeneous earth, *Pure appl. Geophys.*, **128**, 1–6.
- Wyssession, M.E., Lay, T., Revenaugh, J., Williams, Q., Garnero, E.J., Jeanloz, R. & Kellogg, L.H., 1998. The D” discontinuity and its implications, in *The Core-Mantle Boundary Region*, Geodynamic edn, pp. 273–298, ed. Gurnis, M., AGU, Washington D.C.
- Youngs, B.A.R. & Houseman, G.A., 2007. Topography on the D region from analysis of a thin dense layer beneath a convecting cell, *Phys. Earth planet. Inter.*, **160**, 60–74.
- Youngs, B.A.R. & Houseman, G.A., 2009. Formation of steep-sided topography from compositionally distinct dense material at the base of the mantle, *J. geophys. Res.*, **114**, 1–11.

Young, C.J. & Lay, T., 1987. Evidence for a shear velocity discontinuity in the lower mantle beneath India and the Indian Ocean, *Phys. Earth planet. Inter.*, **49**, 37–53.

SUPPLEMENTARY INFORMATION

Additional Supporting Information may be found in the online version of this article:

Figure S1. Filtered beams (with a Butterworth bandpass between 1.0 Hz and 2.0 Hz) formed on PKP_{df} slowness and back-azimuth from seven category 1 events between 135.98° and 136.06° from YKA. Traces are plotted with PKP_{df} at the origin. All traces are normalised to the maximum amplitude within ± 15 s of PKP_{df} .

Figure S2. Additional cross-sections through the scattering ridge in Fig. 8(e), with scattering points, from (a) B to B', across the ridge (scattering points within $\pm 1^\circ$ laterally of the cross-section shown), and from (b) C to C', along the ridge (scattering points within $\pm 0.25^\circ$ laterally of the cross-section shown).

Figure S3. Precursor amplitudes relative to PKP_{df} shown as blue contours as in Fig. 8. Precursors are split into mine source regions

with events from Welkom (south-west) shown as triangles, from Klerksdorp (north-west) shown as squares, and Randfontein and Carletonville (north-east) shown as circles.

Figure S4. Spectrograms calculated using the filtered beam (high-pass filtered at 0.7 Hz with 4 passes) formed on PKP_{df} slowness and back-azimuth for an event on 12/11/1997 with $m_b = 4.5$. Spectrograms are created using (a) short-period, and (b) long-period instrument recordings. The red, green, and pink lines shows the time at which the first precursor, second precursor, and PKP_{df} are picked using the F-pack. Two bright spots can be seen first arriving up to 19s before PKP_{df} which have frequencies of 0.8 Hz and 1.0 Hz with a more blurred third bright spot arriving at the same time with a frequency of 1.9 Hz.

Table S1. Events in data set (<http://gjas.oxfordjournals.org/lookup/suppl/doi:10.1093/gjas/ggt242/-/DC1>)

Please note: Oxford University Press is not responsible for the content or functionality of any supporting materials supplied by the authors. Any queries (other than missing material) should be directed to the corresponding author for the article.